

Copyright
by
Thomas James Bennett IV
2022

The Thesis Committee for Thomas James Bennett IV
certifies that this is the approved version of the following Thesis:

**Development of an Elevated-temperature Tensile Testing
Instrument for Investigating Dynamic Grain Growth in an
Interstitial-free Steel**

APPROVED BY

SUPERVISING COMMITTEE:

Eric M. Taleff, Supervisor

Eric P. Fahrenthold

**Development of an Elevated-temperature Tensile Testing
Instrument for Investigating Dynamic Grain Growth in an
Interstitial-free Steel**

by

Thomas James Bennett IV

THESIS

Presented to the Faculty of the Graduate School of
The University of Texas at Austin
in Partial Fulfillment
of the Requirements
for the Degree of

MASTER OF SCIENCE IN ENGINEERING

THE UNIVERSITY OF TEXAS AT AUSTIN

May 2022

Acknowledgments

I wish to thank my supervisor, Dr. Eric Taleff, for his enthusiasm and extensive involvement in my studies. Dr. Taleff's guidance was instrumental to the success of this project. I would like to thank Adam Kennedy of the Department of Chemistry Glass Shop for the considerable time and effort he devoted to fabricating quartz tubes for this project. I would also like to thank Jamie Svrcek and the Department of Mechanical Engineering Machine Shop staff for fabricating several crucial components for this project and assisting me with machining. The material presented in this thesis is based upon work supported by the National Science Foundation under Grant No. DMR-2003312.

Development of an Elevated-temperature Tensile Testing Instrument for Investigating Dynamic Grain Growth in an Interstitial-free Steel

Thomas James Bennett IV, M.S.E
The University of Texas at Austin, 2022

Supervisor: Eric M. Taleff

Exposure to elevated temperatures during plastic deformation, termed dynamic conditions, produces microstructures distinct from static annealing for a titanium interstitial-free (Ti-IF) steel sheet material. For similar annealing times, dynamic conditions produce larger grains than static annealing and a crystallographic texture that is unique. These differences are attributed to dynamic grain growth (DGG), which occurs by mechanisms different from those of static conditions. The mechanisms of DGG are not yet well understood. The objective of this work is to design and construct a testing instrument suitable for investigations that probe the mechanisms of DGG in Ti-IF steels. This instrument is required to deform a specimen in tension at elevated temperatures in a reducing atmosphere and then rapidly quench that specimen to preserve the microstructure developed during deformation. The instrument was constructed using a servohydraulic tensile test frame, a split

tube furnace, and an original elevated-temperature testing enclosure with reducing gas and air quenching systems. It enabled elevated-temperature tensile tests of Ti-IF steel specimens without significant specimen oxidation. The mechanical data obtained from these tests are in agreement with existing data for the same material. Scanning electron microscopy revealed the presence of preserved subgrain structures in the microstructures of tested specimens. These experimental results confirm that the new instrument satisfies the stated design requirements and is suitable to advance the study of DGG phenomena in Ti-IF steel.

Table of Contents

Acknowledgments	iv
Abstract	v
List of Tables	x
List of Figures	xi
Chapter 1. Introduction	1
1.1 Motivation	2
Chapter 2. Design and Construction of the Elevated-temperature Tensile Testing Instrument	5
2.1 Instrument Design Requirements	6
2.2 Existing Instrumentation	7
2.3 Instrument Design	9
2.3.1 Design Overview	9
2.3.2 Tensile Grips and Load Train	11
2.3.3 Testing Enclosure	11
2.3.4 Forming Gas System	18
2.3.5 Air Quenching System	19
2.3.6 Flow Control Panel	20
2.4 Manufacturing and Assembly	21
2.5 Test Frame Control Software	23
2.5.1 Background of Elevated-temperature Tensile Testing	24
2.5.2 Programming of the Test Control Software	26

Chapter 3. Instrument Characterization and Calibration	29
3.1 Thermal Profiling	30
3.2 Quench System Verification	33
3.3 Performance in a Demonstration Tensile Test	37
Chapter 4. Elevated-temperature Tensile Tests of Ti-IF Steel	38
4.1 Experimental Procedures	39
4.1.1 Tensile Specimen Preparation	39
4.1.2 Elevated-temperature Tensile Testing	40
4.1.2.1 Mechanical Data Processing	43
4.1.2.2 Tensile Testing with Temperature Monitoring	43
4.1.3 Metallographic Sample Preparation	44
4.1.4 Scanning Electron Microscopy	47
4.2 Experimental Results and Discussion	47
4.2.1 Mechanical Testing	47
4.2.2 Metallography	54
Chapter 5. Conclusions and Future Work	59
5.1 Conclusions	59
5.2 Suggestions for Future Work	60
Appendices	62
Appendix A. Technical Drawings	63
Appendix B. Block Diagram and Python Script for Test Software Programming	77
B.1 Multipurpose Elite™ Block Diagram	78
B.2 Python Script for Generating a Displacement Profile	81
B.3 Displacement Profile Header File	83
Appendix C. Python Scripts for Mechanical Data Processing	84
Appendix D. LabVIEW™ Virtual Instrument for Temperature Measurement	103

Appendix E. Forming Gas Flow Meter Data	106
Bibliography	109
Vita	112

List of Tables

3.1	Furnace Controller PID Values	31
4.1	Targeted and Actual True Strains for Tests Performed	38
4.2	The composition of the Ti-IF steel sheet, as provided by the supplier, is listed in weight percent.	39
4.3	The grinding and polishing steps used to prepare Ti-IF steel specimens for metallography are listed.	46
E.1	The flow meter marker locations and corresponding flow rates for N ₂ provided as reported by Brooks Instrument for part number 60410_R5.106	

List of Figures

2.1	The tensile specimen geometry is shown with dimensions given in inches. The nominal specimen thickness is 0.0272 inches.	6
2.2	This photograph shows the MTS 810 test frame (1), 100 kN load cell (2), cooling couplings (3), ATS 3210 split-tube furnace (4), and furnace controller (5) before the installation of the new fixtures. The 10 kN load cell is not installed in this photograph.	8
2.3	This rendering shows an overview of the testing enclosure and associated hardware with primary components labeled.	10
2.4	This schematic shows (a) an exploded view of the upper stop assembly and (b) a cross-section view of the upper stop assembly inserted into the upper end of the quartz tube. Air quench and exhaust tubes are hidden for clarity. The figure is not to scale.	13
2.5	This schematic shows (a) an exploded view of the lower stop assembly and (b) a cross-section view of the lower stop assembly attached to the lower pull-rod and bellows. The figure is not to scale.	17
2.6	The heat shielding baffles and the locations of the quench air holes are shown in this rendering. The quartz tube is hidden for clarity.	19
2.7	This photograph shows the flow control panel for the cooling water, forming gas, and quench air attached to the MTS 810 test frame.	21
2.8	This photograph shows the completed assembly of the tensile fixture attached to the MTS 810 test frame.	22
3.1	Specimen thermocouple temperature is plotted against the controller thermocouple temperature. The linear regression line and its corresponding equation are provided. The open circle indicates the measurement taken at a setpoint of 837 °C for verification.	32
3.2	The dummy specimen temperature is plotted against time starting at the activation of the air quenching system. The initial specimen temperature was 850 °C.	34
4.1	This photograph shows the thermocouple attached to the specimen gauge region for the sixth tensile test.	44

4.2	(a) The dashed lines in the schematic indicate how each tensile specimen was sectioned for metallography. The arrows on sections 1 and 3 indicate the surfaces visible in the mount. (b) This schematic depicts the layout and orientation of each sectioned piece in a single mount. Note that “•” and “×” represent arrows out of and into the page respectively.	45
4.3	Scanned images of a specimen are shown (a) before and (b) after testing. Pin-hole elongation is apparent in the upper grip region of the tested specimen. The darkened region at the center of the gauge region in (b) is from modest oxidation by the pressurized air used for quenching.	49
4.4	True strain data from the fifth tensile test are plotted as a function of time. A linear regression line is also plotted.	50
4.5	True stress and true strain data from the fifth tensile test are plotted. The flow stress behavior shown is representative of that observed in all other tests.	51
4.6	(a) The measured specimen temperatures are plotted against quenching time. (b) The first 20 seconds of quenching shows the initial temperature drop. The line at 727 °C indicates where the creep rate would decrease by a factor of 100, as calculated in Section 3.2. The legend applies to both plots.	52
4.7	This BSE photomicrograph shows the microstructure in the TD-TLTD plane of the third specimen tested. The microstructure shown is representative of all specimens tested in tension.	55
4.8	This BSE photomicrograph, taken in the TD-TLTD plane, shows apparent subgrains in the microstructure of the third specimen tested. Examples of apparent subgrain boundaries are labeled as “SGB.”	56
4.9	Lineal intercept grain sizes are plotted against true strain. The grain size measurements are from photomicrographs of the TD-TLTD plane taken at (a) 200× and (b) 500×. The recrystallized grain size is indicated by the shaded region. The error bars and the shaded region represent the 95% confidence intervals of the measurements.	58
A.1	Shown is the technical drawing for the lower pull-rod.	64
A.2	Shown is the technical drawing for the lower sheath.	65
A.3	Shown is the technical drawing for the lower stop.	66
A.4	Shown is the technical drawing for the lower stop assembly.	67
A.5	Shown is the technical drawing for the upper pull-rod.	68
A.6	Shown is the technical drawing for the upper sheath.	69
A.7	Shown is the technical drawing for the upper stop.	70

A.8	Shown is the technical drawing for the upper stop assembly.	71
A.9	This technical drawing shows the tube geometry for the upper stop assembly.	72
A.10	Shown is the technical drawing for the quartz retort.	73
A.11	Shown is the technical drawing for the flow control panel.	74
A.12	Shown is the technical drawing for the base brace. This is used to mount the flow control panel to the test frame.	75
A.13	Shown is the technical drawing for the flow control panel assembly.	76
B.1	Shown is the MTS Multipurpose Elite™ software block diagram for elevated-temperature tensile testing (Part 1).	78
B.2	Shown is the MTS Multipurpose Elite™ software block diagram for elevated-temperature tensile testing (Part 2).	79
B.3	Shown is the MTS Multipurpose Elite™ software block diagram for elevated-temperature tensile testing (Part 3).	80
D.1	The front panel of the LabVIEW™ virtual instrument is shown.	104
D.2	The block diagram for the LabVIEW™ virtual instrument is shown.	105

Chapter 1

Introduction

Many important physical properties of metals at the macroscopic scale are controlled by microstructure. In particular, the mechanical properties of metals are strongly dependent on grain morphology and crystallographic texture, which is the distribution of crystallographic orientations for grains in the material. Additionally, the mechanical properties of metal alloys can be strongly influenced by the morphology and distribution of secondary phases. However, in the engineering of single-phase metals and alloys, grain size and crystallographic texture are controlled to achieve desired material properties. Grain size and texture are most often controlled through combinations of annealing processes and deformation called thermomechanical processing [1].

Annealing processes may be performed under either static or dynamic conditions. The distinction between the two is the presence of concurrent plastic deformation, here termed as dynamic conditions. The addition of plastic deformation typically alters the recovery, recrystallization, and grain growth phenomena that take place during annealing. Concurrent deformation during grain growth produces significant differences in grain size and texture compared to a similar annealing process performed under static conditions [1, 2]. This leads to a natural classification of grain

growth into the categories of static grain growth (SGG) and dynamic grain growth (DGG). One key feature of DGG is that the rate of grain growth is often more rapid than that of SGG [2].

Grain growth may be alternatively classified as either normal grain growth (NGG) or abnormal grain growth (AGG). AGG is characterized by the presence of one or a few grains that grow at a much faster rate and to a much larger size than surrounding “normal” grains. On the contrary, normal grain growth, as the name implies, is grain growth without the formation of abnormal grains. These two methods of classifying grain growth may be combined to give the following four distinct grain growth classifications: static normal grain growth (SNGG), static abnormal grain growth (SAGG), dynamic normal grain growth (DNGG), and dynamic abnormal grain growth (DAGG).

1.1 Motivation

Many forms of metals processing utilize high-temperature deformation. A thorough understanding of the microstructural evolution during these processes requires a fundamental understanding of DGG phenomena. In particular, an understanding of DNGG is necessary to meaningfully predict and control microstructural evolution during high-temperature processes such as hot rolling or extrusion. This is of interest in the production of materials that benefit from or require specially engineered crystallographic textures. One example of such a material is high-modulus steel sheet that is desired for reducing the mass of automotive components without sacrificing overall part stiffness. These steel sheet materials have strong $\{110\}\langle 111\rangle$ to

$\{110\}\langle 112 \rangle$ and $\{112\}\langle 111 \rangle$ texture components and consequently have Young's moduli along the rolling direction up to 10% larger than that of conventional steels [3]. Another application that could benefit from an understanding of DGG phenomena is the production of Fe-Si steel sheet for transformer cores. For these materials, textures with strong $\{110\}\langle 001 \rangle$ components are preferred because the $\langle 001 \rangle$ directions are easiest to magnetize [4, 5].

Many aspects of DGG are generally not well-understood. In particular, the specific mechanisms by which DNGG and DAGG occur are not well developed. As a consequence, the factors that determine the onset or inhibition of DNGG and DAGG are not understood. These factors include material characteristics, such as crystal structure, alloying elements, and impurity content, as well as characteristics of the material deformation, such as deformation rate and temperature. While the effects of several material and deformation related factors on DGG phenomena have been empirically determined, a complete description in terms of fundamental mechanisms has not yet been formulated. The potential to better understand the fundamental mechanisms responsible for DGG and the relevance to a wide array of metals processing applications motivates the continued study of DGG phenomena.

Prior work on DGG was based on the results of hot uniaxial tensile experiments conducted on interstitial-free (IF) steels alloyed with small amounts of Ti, otherwise known as Ti-IF steel [2, 6]. Only DNGG was observed in Ti-IF steel in previous work. These hot uniaxial tensile tests were conducted either under vacuum or in air. Both methods of hot-tensile testing were subject to distinct experimental limitations. Tensile specimens tested under vacuum could not be cooled rapidly enough to provide

confidence that important features of the deformed microstructure were preserved. The tensile specimens tested in air could be cooled rapidly but underwent severe and rapid oxidation that degraded the mechanical test data collected [2].

In order to continue investigating DNGG phenomena in Ti-IF steels and similar materials, a new hot-deformation testing instrument capable of preventing oxidation at high temperatures and adequately quenching test specimens for the preservation of microstructure is necessary. The goal of the present work is to develop, manufacture, and verify the successful operation of such an instrument. This includes reproducing the combined results of hot tensile tests performed under vacuum and in air by Noell and Rupp [2, 6, 7].

Chapter 2

Design and Construction of the Elevated-temperature Tensile Testing Instrument

The study of DGG behavior in Ti-IF steels requires an experimental instrument capable of deforming a specimen in tension at elevated temperatures and rapidly quenching that specimen while maintaining an applied load. This instrument must protect the specimen from oxidation while at the elevated temperature. Previous experiments on Ti-IF steels were conducted at elevated temperatures either under vacuum or in air using two different tensile testing instruments. Both test instruments had experimental limitations distinct from those of the other. The tests performed under vacuum were limited by the inability to rapidly cool specimens from elevated temperature. A consequence of slow cooling rates was inadequate preservation of microstructures developed during deformation at elevated temperatures [2]. Tests performed in air enabled rapid cooling after testing but were limited by severe oxidation of the specimen while at elevated temperatures. This rapid oxidation caused the cross-sectional area of the specimen to reduce, preventing accurate stress measurements [2]. In order to perform experiments that provide both rapid quenching and oxidation protection, a new instrument is necessary.

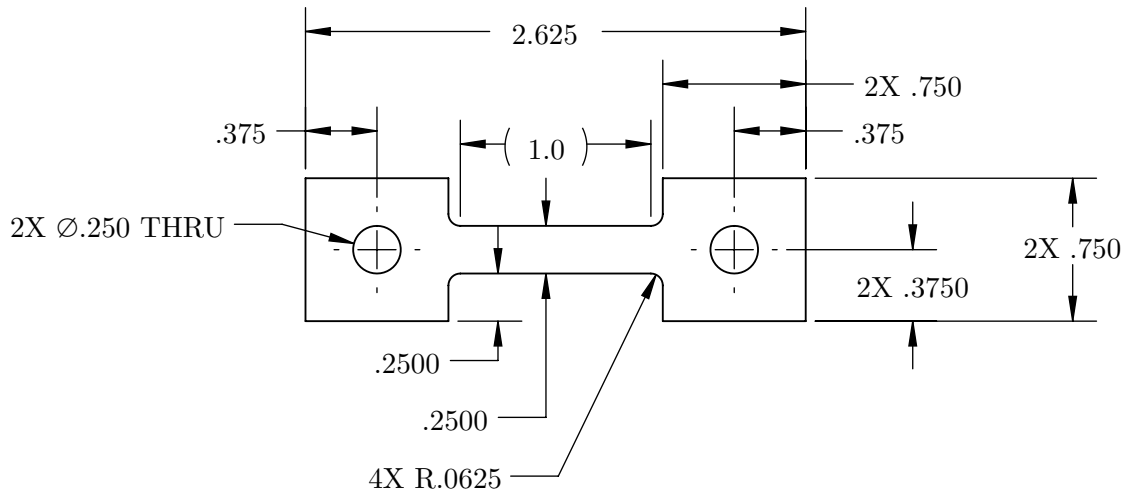


Figure 2.1: The tensile specimen geometry is shown with dimensions given in inches. The nominal specimen thickness is 0.0272 inches.

2.1 Instrument Design Requirements

The new instrument is required to deform a specimen of Ti-IF steel in uniaxial tension at a constant true-strain rate and at elevated temperatures below the critical temperature for the transformation from ferrite to austenite. For the Ti-IF steel used in the present study, this temperature is approximately 892 °C [2]. The instrument must protect the test specimen from oxidation at elevated temperature with a suitable inert or reducing gas environment. The instrument must also be able to rapidly quench the test specimen while holding it under a tensile load following a tensile test. This is to preserve the microstructure developed during testing. The specimen geometry for this study is shown in Figure 2.1.

In addition to the requirements just described, the instrument should also enable the user to safely, easily, and repeatably perform tensile tests at elevated

temperatures. Compressed gases used for oxidation prevention and air quenching must be properly regulated and exhausted from the instrument. The instrument design must include mechanisms for safe pressure relief. Components sensitive to high temperatures must be shielded or cooled to prevent overheating. The tensile fixtures, particularly the specimen grips, must be easily accessible for specimen insertion and removal. Test parameters (strain rate, temperature, time-at-temperature, quench rate, etc.) must be easily adjustable and repeatable between tests.

2.2 Existing Instrumentation

The foundation of the instrument is a Material Test Systems (MTS) 810 servohydraulic tensile test frame. This test frame is computer-controlled using an MTS FlexTest 40TM digital controller and MTS TestSuiteTM Multipurpose Elite (version 4.5.2.423) control software. The test frame is equipped with a 100 kN (22 kip) load cell and 10 kN (2.2 kip) load cell installed in series. The finer force resolution of the 10 kN load cell is necessary to measure the low tensile loads expected during elevated-temperature testing. The test frame is also equipped with water-cooled couplings located at the top and bottom of the tensile load train. The water-cooled couplings prevent heat conducted along the pull-rods from overheating the load cells and hydraulic components of the test frame. An Applied Test Systems (ATS) series 3210 split-tube three-zone furnace is mounted to the test frame and encloses the central region of the tensile load train. The heating zones of the split-tube furnace encompass a 16-inch-long cylindrical region 3 inches in diameter. The furnace is controlled by a 30-amp ATS Series 3000 Three Zone Temperature Control System and

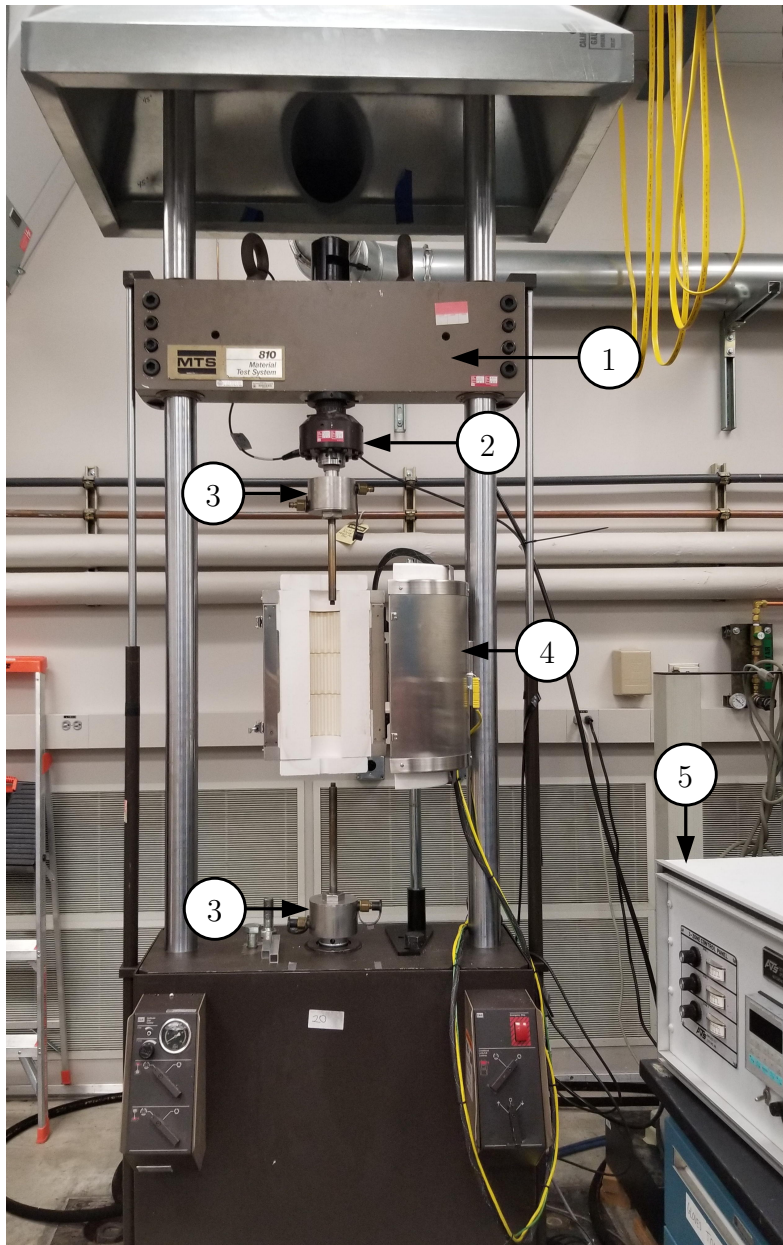


Figure 2.2: This photograph shows the MTS 810 test frame (1), 100 kN load cell (2), cooling couplings (3), ATS 3210 split-tube furnace (4), and furnace controller (5) before the installation of the new fixtures. The 10 kN load cell is not installed in this photograph.

has a maximum operating temperature of 1200 °C. The MTS 810 test frame and the attached ATS 3210 split tube furnace are shown in Figure 2.2.

2.3 Instrument Design

2.3.1 Design Overview

The high-temperature tensile testing instrument is composed of tensile grips; pull-rods; a testing enclosure; delivery and exhaust systems for reducing gas and quenching air; and a cooling system. The testing enclosure is a cylindrical retort centered along the tensile loading axis that fits within the split-tube furnace and surrounds the tensile grips. A N_2 -4% H_2 forming gas, selected as the protective gas, fills the retort during elevated temperature testing to protect the tensile specimen from oxidation. The retort connects to a flexible bellows that accommodates the motion of the test frame piston and functions as a gas seal. The enclosure can be quickly separated at the bellows and lifted for access to the tensile grips. The quenching system rapidly cools tensile specimens using jets of air that impinge on the specimen. Air also flows from the bottom of the retort. The gas exhaust system directs forming gas and quench air from the enclosure into a fume hood above the test frame. The cooling system utilizes chilled water to prevent temperature-sensitive components of the instrument from overheating. A schematic overview of the gas retort and associated hardware is shown in Figure 2.3.

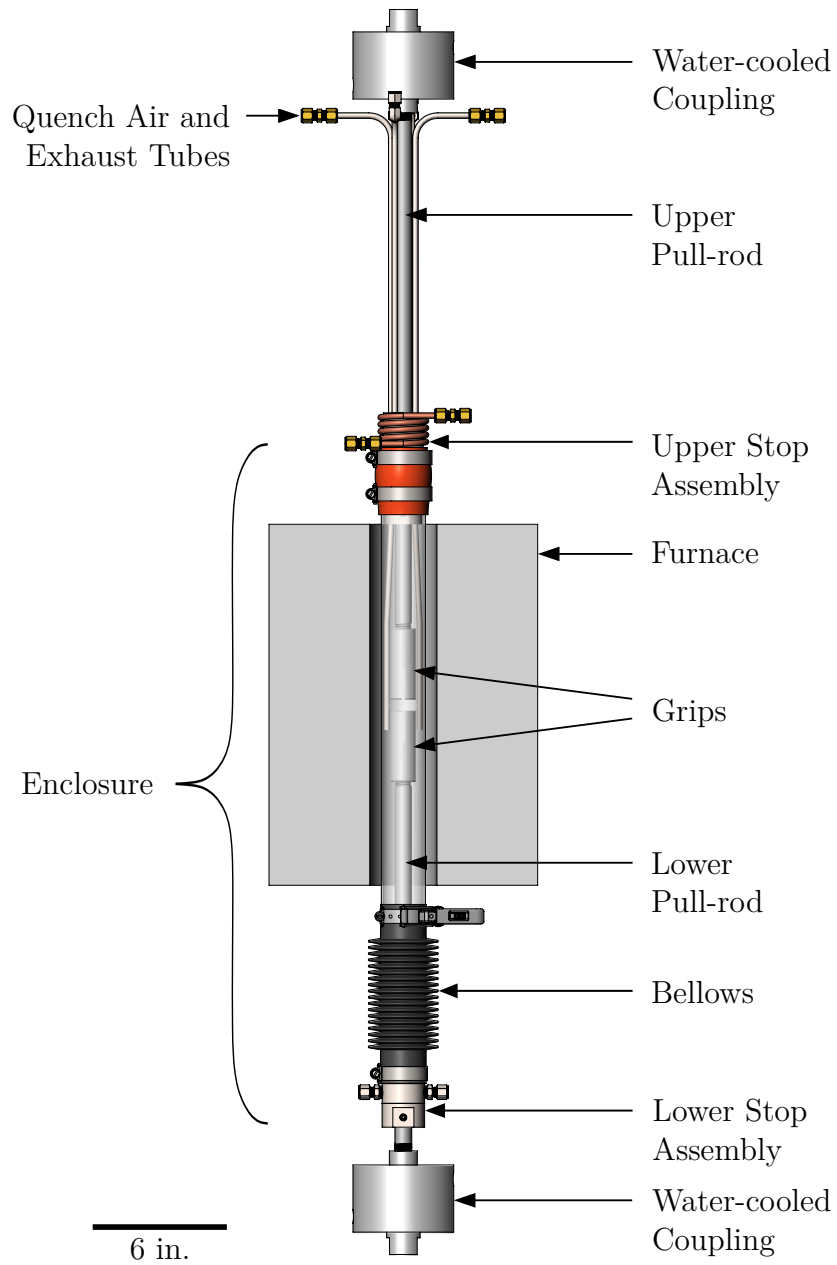


Figure 2.3: This rendering shows an overview of the testing enclosure and associated hardware with primary components labeled.

2.3.2 Tensile Grips and Load Train

The tensile pull-rods are made of $\frac{3}{4}$ -inch diameter nickel alloy 625 round bar. Nickel alloy 625 (trade name Inconel 625) was chosen as the pull-rod material for its high strength at elevated temperatures and relatively low thermal conductivity (9.8 W/m · K compared to around 70 W/m · K for commercially pure nickel) [5, 8]. The pull-rod lengths were chosen to satisfy the geometric requirements of the test frame and forming gas enclosure. The upper pull-rod length is the minimum necessary to lift the gas retort above the upper tensile grip. This allows the user to interchange tensile specimens without disassembling the enclosure. The lower pull-rod length was chosen in accordance with the upper pull-rod to fit within the vertical space of the test frame and allow suitable piston motion for testing. Unified National $\frac{3}{4}$ -inch fine and coarse threads were machined onto opposite ends of both pull-rods for connections with the water-cooled couplings and tensile grips, respectively. Technical drawings of the pull-rods are provided in Appendix A. Inconel pin-loading tensile grips are used to fix the tensile specimens within the load train. The tensile specimens are attached to the grips and loaded by $\frac{1}{4}$ -inch diameter pins.

2.3.3 Testing Enclosure

The gas retort is a tube of fused quartz, 540 mm long (21.3 in), with nominal inner and outer diameters of 46 mm (1.81 in) and 50 mm (1.97 in) respectively. The quartz tube is supported from its upper end by an assembly of parts, henceforth known as the upper stop assembly, that mounts to the upper pull-rod. Tubes for air quenching and gas exhaust pass into the quartz tube through the upper stop

assembly. The upper stop assembly seals against the inner surface of the quartz tube with two O-rings. The upper end of the quartz tube is lightly flared, thickened, and flame polished to remove defects that could lead to fracture under the tensile stresses imposed by the O-rings. The light flare reduces the effort required to insert the seal-bearing component of the upper stop assembly into the quartz tube.

The bottom end of the quartz tube interfaces with an assembly of parts, henceforth known as the lower stop assembly, that mounts to the lower pull-rod. The lower stop assembly functions as an inlet for the forming gas and additional quench air. Because the lower pull-rod is mobile, a neoprene rubber bellows is used to seal the lower stop assembly with the quartz tube. The bellows seals around the outer surface of the quartz tube with a quick-release hose clamp, which allows the user to easily detach it during specimen insertion and removal. Because the lower end of the quartz tube can exceed the maximum operational temperature of neoprene rubber, a strip of high-temperature silicone rubber sheet is inserted under the rubber bellows at the hose-clamp connection as insulation. A hose clamp seals the other end of the bellows around the outer surface of the lower stop assembly. The bottom of the quartz tube is flared outward, which guides the tube over the lower grips and pull rod when it is lowered following specimen installation. This flare also stretches the bellows in the circumferential direction to create a seal sufficiently tight to prevent leakage of forming gas or quench air.

The upper stop assembly, depicted schematically in Figure 2.4, is composed of two primary components machined from stainless steel alloy 316: the “upper stop” and “the upper sheath”. The upper stop is a cylindrical collar through which the

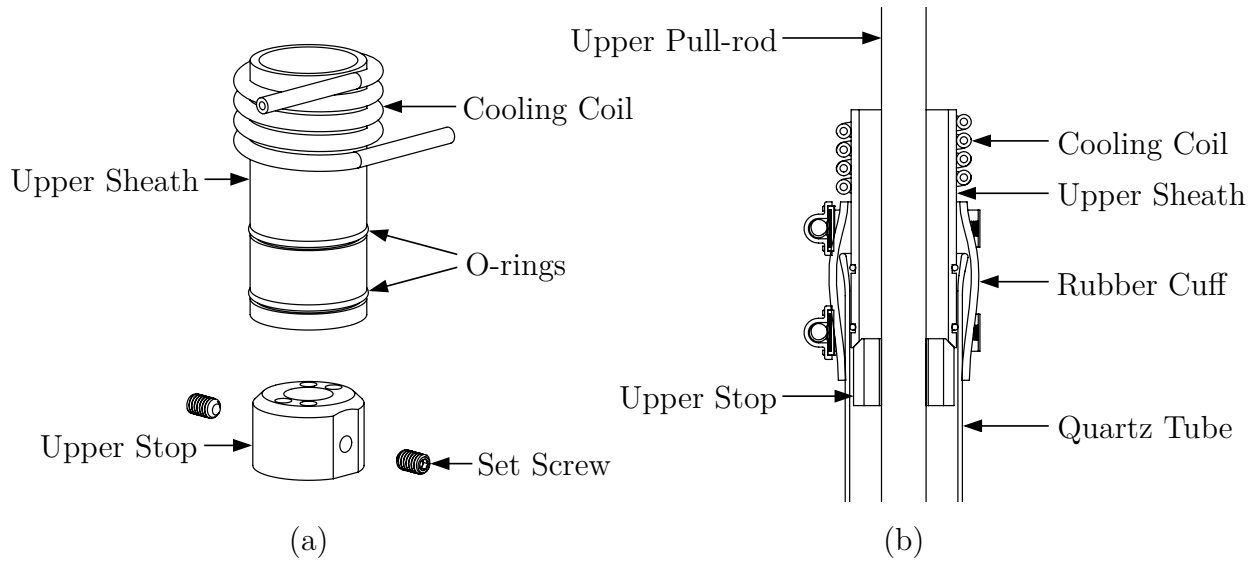


Figure 2.4: This schematic shows (a) an exploded view of the upper stop assembly and (b) a cross-section view of the upper stop assembly inserted into the upper end of the quartz tube. Air quench and exhaust tubes are hidden for clarity. The figure is not to scale.

upper pull-rod passes. The diameter of this passage hole is machined to a nominal size approximately 0.002 inches larger than the diameter of the pull-rod to create a close clearance fit. This clearance fit gap allows the upper stop to slide along the pull-rod for ease of assembly and is small enough to prevent significant leakage of forming gas from the testing enclosure.

The upper stop is rigidly mounted to the upper pull-rod by two opposing set screws and fits inside the quartz tube. Four holes drilled into the upper stop function as ports for gas exhaust and quench air inlets. These holes are drilled to a nominal diameter of 0.257 inches (standard F drill size) to allow the passage and brazing of $\frac{1}{4}$ -inch stainless steel tubing. The resulting gap size of approximately 0.0035 inches

between the upper stop and the stainless steel tubing was intentionally selected to match recommended clearances for brazing [9]. This gap size is critical because it allows capillary action to draw the filler metal into the joint during brazing.

When assembled, the upper stop is located outside of the split tube furnace. Despite this, the upper stop will reach high-temperatures because it is connected to the upper pull-rod, which extends into the center of the furnace. Because the upper stop will reach high temperatures during operation, a high-melting point silver alloy 50 (BAg-1a) braze was selected as the filler metal. The solidus temperature of silver alloy 50 is 630 °C [10]. Because the upper stop is located far away from the center of the furnace, it is not expected to exceed the solidus temperature of the braze. Heat shielding, described next, and water cooling on the upper sheath provide additional protection against overheating the upper stop.

To reduce heat transfer to the upper stop by radiation and convection, heat shielding baffles are attached to the upper pull-rod between the grip and the upper stop. These baffles are shown in Figure 2.6. The baffles are cut from 0.003-inch thick nickel 200 shim stock. A hole and two slots are cut into the baffles to allow them to fit over the upper pull-rod and the quench air lines. The baffles are corrugated to improve their rigidity. This corrugation creates a slight interference with the pull-rod, which helps the baffles stay in place through friction. To lower the resistance to air flow during quenching, holes are cut into the baffles. To prevent convection plumes from forming during elevated-temperature testing, these holes alternate in angular position between adjacent baffles.

The upper sheath is a hollow cylinder with two O-ring grooves machined into

its outer surface. Two soft high-temperature silicone O-rings fit into the grooves and seal against the inner surface of the quartz tube. The upper sheath rests on top of the upper stop and suspends the quartz tube by friction from the O-ring seals. A silicone rubber cuff attaches around the outer surfaces of the quartz tube and the upper sheath with two hose clamps to provide a second means of supporting the weight of the tube. The hose clamp around the quartz tube is just tight enough to support its weight. This avoids placing undue stress on the quartz tube.

Opposing 45° conical faces are machined into the top face of the upper stop and the bottom face of the upper sheath. These opposing conical faces align the center-lines of the upper stop and the upper sheath. This aligns the quartz tube with the upper pull-rod. In addition to alignment, this conical interface acts as a low-pressure seal between the upper stop and the upper sheath and provides a safe pressure relief point. In circumstances where the enclosure might become pressurized (i.e. during air quenching), the quartz tube and the upper sheath can lift upwards to relieve that pressure. This method of pressure relief ensures that explosive pressures cannot build within the quartz tube.

Considerations of temperature and sealing force guided the selection of the O-rings and the design of the grooves in the upper sheath. A comparison of the nominal quartz tube inner diameter with recommended bore sizes provided in a static radial seal chart (see Ref. [11]) yielded dash number 130 as the most appropriate O-ring size. The O-ring groove diameter was reduced from the recommended value provided in the radial seal chart to obtain a circumferential stretch ratio of 1%. This falls within the range of 1-5% recommended for an effective seal. Durometer 50A silicone

was selected as the O-ring material because it is relatively soft, which reduces the sealing force, and can withstand temperatures up to 200 °C [11]. Minimizing the circumferential stretch of the O-rings reduces the sealing force exerted on the quartz tube. The interested reader is referred to Ref. [11]¹ for guidelines and more details regarding O-ring design.

A water cooling coil is attached at the top end of the upper sheath to regulate the temperature of the O-rings, the rubber cuff, and the upper stop. The cooling coil was formed by clamping the upper sheath in a lathe chuck and manually wrapping 1/4-inch diameter copper tubing around it. The lathe power was disconnected during the wrapping operation. Only four complete wraps were formed to allow enough space for the attachment of the rubber cuff. After the coil was formed, JB Weld™ steel-reinforced epoxy was applied between the upper sheath and the cooling coil to create a bond and improve heat conduction. Chilled water is passed to and from the cooling coil through 1/4-inch diameter polyethylene tubing connected with compression fittings. The cooling coil is installed in parallel with the upper and lower cooling couplings, shown in Figure 2.3, in the chilled water circulation system.

The lower stop assembly, depicted schematically in Figure 2.5, is composed of two stainless steel 316 parts: the “lower stop” and the “lower sheath”. Like the upper stop, the lower stop is a collar that fits around the lower pull-rod and is fixed by two set screws. A nominal clearance of 0.002 inches allows the lower stop to freely slide along the pull-rod for ease of assembly. The lower sheath is a hollow cylinder with two

¹A digital version of this reference is available at: <https://www.applerrubber.com/src/pdf/seal-design-guide.pdf>.

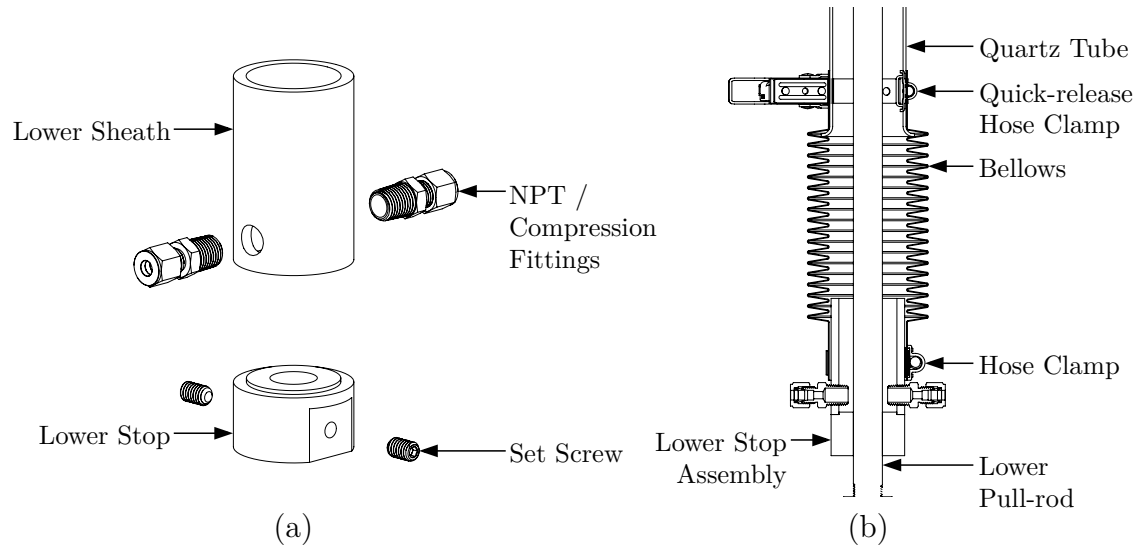


Figure 2.5: This schematic shows (a) an exploded view of the lower stop assembly and (b) a cross-section view of the lower stop assembly attached to the lower pull-rod and bellows. The figure is not to scale.

threaded holes machined into its sides. The threads are $\frac{1}{4}$ -inch National Pipe Thread (NPT) for the attachment of standard compression tube fittings. Forming gas and quench air enter the enclosure through these fittings. The lower sheath is sealed to the lower stop by a complete circumferential seam weld. The rubber bellows attaches to the top of the lower sheath using a hose clamp. A piece of silicone rubber sheet is inserted between the hose clamp and the bellows to create a seal and protect the bellows from damage by the screw mechanism on the hose clamp. Detailed technical drawings of the parts designed for the instrument are provided in Appendix A.

2.3.4 Forming Gas System

The forming gas system is an integral part of the high-temperature tensile instrument because it satisfies the design requirement for oxidation protection. The forming gas system is comprised of three main components: the compressed gas cylinder, the gas entry system, and the exhaust lines. Nitrogen-based forming gas (4% H₂, bal. N₂, NI HY4C-K) was selected as the protective gas for Ti-IF steel testing. Hydrogen is present to act as a reducing agent, which reacts with oxide-forming impurities [12]. This provides enhanced oxidation protection compared to nitrogen alone. A 4% hydrogen mixture was selected because it falls below the hydrogen flammability limit at room temperature [13].

The forming gas is regulated to 20 psig by a dual-stage CGA 350 pressure regulator and is routed to the testing instrument through 1/4-inch polyethylene tubing. The forming gas line is connected to an adjustable flow meter that controls the flow rate between 0 and 900 cc/min. This adjustable flow meter indicates the flow of forming gas and allows the flow rate to be set to completely displace the air in the enclosure before reaching elevated temperatures. Another 1/4-inch polyethylene tube directs the forming gas from the adjustable flow meter to the lower stop assembly, where it enters the testing enclosure.

The exhaust system consists of two 1/4-inch 316 stainless steel tubes that extend upwards from the upper stop. The exhaust tubes are bent at right angles away from the upper pull-rod to allow the attachment of compression fittings. Polyethylene tubes attached to these compression fittings route the forming gas directly into the fume hood located above the MTS 810 test frame. Because the right angle bends

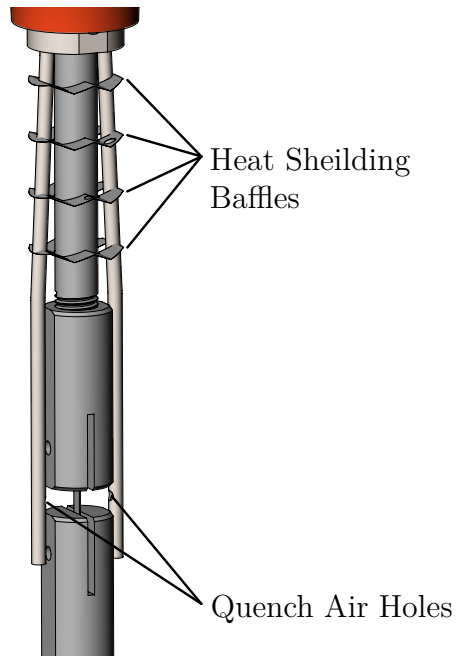


Figure 2.6: The heat shielding baffles and the locations of the quench air holes are shown in this rendering. The quartz tube is hidden for clarity.

limit the travel of the quartz tube, they were placed sufficiently far from the upper stop to allow the quartz tube to be lifted above the upper tensile grip.

2.3.5 Air Quenching System

The air quenching system directs clean pressurized air into the testing enclosure to rapidly cool the tensile specimen and preserve its microstructure following a tensile test. The quench air is introduced into the enclosure from two locations: adjacent to the specimen and at the lower stop assembly. Air jets are directed towards the specimen by two 316 stainless steel tubes that enter the enclosure through the upper stop. The ends of these quench air tubes inside the enclosure are pinched

and welded shut to prevent air from being directed below the specimen. Two $\frac{1}{8}$ -inch holes are drilled into the inward facing sides of the quench air tubes to direct air towards opposite sides of the specimen gauge region. The tubes are slightly bent to fit around the upper tensile grip. The positions of the air holes and the bent shapes of the tubes are shown in Figure 2.6. The ends of the quench air tubes outside the enclosure are bent at right angles, in the same manner as the exhaust tubes, to enable the attachment of compression fittings.

Air is directed through the lower stop assembly and the bottom of the enclosure during quenching to prevent hot air from flowing downward and overheating the neoprene rubber bellows. The quench air is sourced from the building's pressurized clean air system and is regulated to 30 psig. The quenching system is activated by a manually operated fast-acting valve. The quench air exits the testing enclosure through the exhaust lines for the forming gas.

2.3.6 Flow Control Panel

The adjustable flow valve for controlling the forming gas flow rate and the fast-acting valve for the air quenching system are mounted in a custom control panel. A frame composed of aluminum T-slotted extrusions mounts to the MTS 810 test frame and supports the flow control panel. The position of the flow control panel relative to the test frame allows the operator to quickly and easily control the flow of gases during testing while maintaining a safe distance from the furnace. The flow control panel also includes a flow indicator with an adjustable valve for the water cooling coil on the upper sheath. A photograph of the control panel mounted to the



Figure 2.7: This photograph shows the flow control panel for the cooling water, forming gas, and quench air attached to the MTS 810 test frame.

MTS 810 frame is shown in Figure 2.7. Technical drawings for the control panel parts and assembly are listed in Appendix A.

2.4 Manufacturing and Assembly

The Mechanical Engineering Machine Shop brazed the stainless steel tubing and machined the pull-rods and stainless steel components. The Chemistry Department Glass Shop cut, flame polished, and flared the fused quartz tube. The machining of additional parts, bending of the stainless steel tubes, and assembly of the instrument were completed by the author. A photograph of the assembled instrument is shown in Figure 2.8.



Figure 2.8: This photograph shows the completed assembly of the tensile fixture attached to the MTS 810 test frame.

During the assembly of the quench air and exhaust tubes, the order of operations was critical for the successful assembly of the instrument. First, the unbent stainless steel tubes were cut to the proper lengths and brazed to the upper stop. The tubes were brazed in predetermined positions relative to the upper stop as specified in a technical drawing (see Appendix A, Figure A.8). The ends of the quench air tubes inside the enclosure were pinched and seam welded after brazing. Next, the upper sheath was passed over the quench air and exhaust tubes so that its conical face matched the opposing conical face on the upper stop. At this point, the water cooling coil had been formed and bonded to the upper sheath. Once the upper sheath was in place, the top ends of the quench air and exhaust tubes were bent at right angles with a bend radius of one inch. After this tube bending operation, the upper sheath became inseparable from the assembly. Next, the specimen-adjacent portions of the quench air tubes were bent to fit around the upper tensile grip. These bend geometries are shown in Figure A.9 in Appendix A. The drilling of the air holes directed at the tensile specimen was completed last. To ensure proper placement of these holes, their desired locations were measured with all the components assembled on the test frame.

2.5 Test Frame Control Software

The motion of the hydraulic piston on the MTS 810 test frame is computer controlled using several programs developed by MTS. Tensile test routines are programmed and executed using the MTS TestSuiteTM Multipurpose Elite (MPE) software (version 4.5.2.423). To satisfy the design requirement for uniaxial deformation

at a constant true-strain rate, a test routine was programmed to implement constant true-strain rate control in the MPE software. In addition to this, the test routine was designed to accommodate the unique requirements of elevated-temperature testing. These requirements, and other background information necessary to understand the test routine design, are provided in the next section.

2.5.1 Background of Elevated-temperature Tensile Testing

Elevated-temperature tensile tests using a furnace consist of three segments: heat-up, deformation, and cool-down. During heat-up, the specimen is heated to the testing temperature. As the temperature of the load train (the specimen, grips, and pull-rods) increases, it thermally expands. To prevent the specimen from being compressed, the test frame piston must move to accommodate the thermal expansion of the load train. This is accomplished by using force control to hold a constant tensile load on the specimen during heat-up. This load must be large enough to be detected by the load cell but small enough to avoid unnecessary creep deformation before the intended deformation.

During deformation, the specimen is strained to either failure or a target strain value. At elevated temperatures, particularly those for which the homologous temperature is above 0.4, deformation by creep becomes significant [14]. In the temperature regime for creep, the deformation rate is typically controlled to achieve a constant true-strain rate. This facilitates the subsequent analysis of creep behavior. For the present work, tests were only performed at a constant true-strain rate to a predetermined true-strain value, less than the strain for failure.

To achieve constant true-strain rate control, the displacement rate imposed by the test frame must be continuously updated for the current specimen gauge length. An expression giving the specimen elongation rate in terms of its current gauge length and the desired true-strain rate may be obtained by starting with the definition for an increment in true strain:

$$d\varepsilon = \frac{dL}{L}. \quad (2.1)$$

Here, ε represents true strain and L represents the gauge length of the specimen in the current configuration. Dividing Equation 2.1 by a small time increment dt and rearranging yields

$$\frac{dL}{dt} = L \frac{d\varepsilon}{dt}, \quad (2.2)$$

which is the desired relation. By assuming that the deformation of the load train and the specimen grip regions are negligible compared to the elongation of the gauge region, the rate of extension dL/dt can be taken as equal to the displacement rate of the piston. With this assumption, Equation 2.2 can be used in control software to obtain a constant true-strain rate using displacement control.

During cooldown, the specimen is cooled to room temperature and then extracted. To accommodate thermal contraction, a constant force is placed on the specimen using force control. For the present study, it is of interest to preserve the subgrain microstructure produced in the specimen during deformation at elevated temperature. To preserve the microstructure, the specimen is rapidly air quenched while applying the final tensile load from the deformation segment.

2.5.2 Programming of the Test Control Software

The test routine programmed in the control computer is divided into five steps. The block diagram for the test routine, as shown in the MPE software, is provided in Appendix B.1. Force and displacement data are continuously acquired at a sampling frequency of 10 Hz during each of the five steps. A log message is written following each step to confirm the successful completion of that step of the routine. Step 1 removes any slack in the load train. The piston is displaced at a constant rate of 0.005 mm/s until the tensile load reaches 10 lbf. Then, the tensile load is reduced to 1 lbf using a 10-second ramp in force control mode. This is done because a tensile load of 1 lbf is insufficient to remove all the initial slack in the load train but is sufficient to maintain a taut load train while avoiding creep deformation during heating. Once the target load of 1 lbf is reached, the control software automatically offsets the displacement channel to zero and proceeds to Step 2. The control mode is changed from displacement to force control for Step 2.

Step 2 maintains a load of 1 lbf on the tensile specimen during heat-up and temperature stabilization. A constant force command (termed “dwell” in the software) is repeated until the user selects a virtual button in the graphical user interface to manually indicate the end of Step 2. The control software then switches from force control to displacement control, offsets the displacement channel to zero, and proceeds to Step 3. Note that the displacement measurements should ideally be adjusted in post-processing to account for the elastic elongation of the specimen under the applied load of 1 lbf. However, this adjustment is typically insignificantly small.

Deformation at a constant true-strain rate is executed in Step 3. The displacement rate of the piston is continuously updated from a look-up table based on the present displacement to provide a constant true-strain rate. A Python script was written to generate look-up tables for any constant true-strain rate and specimen gauge length before starting a test. This script generates, using Equation 2.2, a table containing displacement rates for displacements increasing from zero in increments of 0.1 mm. The script writes the table to a text file with the file extension “.blk” so that it can be imported by the MPE software. The Python script is provided in Appendix B. Step 3 automatically ends when the piston displacement reaches a predefined target value that the user must input before running the control routine. Step 3 ends before the target displacement if the user selects a virtual button to manually terminate this step. Note that a “dwell” command is issued in displacement control for one second at the start of Step 3. This ensures that the MPE software properly switches from force control mode to displacement control mode. Unlike other commands in the software, the previously described look-up table command (termed “profile” in the software) does not automatically switch to the appropriate control mode before execution.

Step 4 holds the final tensile load from Step 3 on the specimen as it is quenched. A “dwell” command is issued in force control mode to hold the current load. Like Step 2, this command for Step 4 is repeated until the user selects a virtual button to manually indicate the end of the quenching process and start Step 5. Step 5 removes the tensile load on the specimen so it can be removed from the grips. The load on the specimen is reduced to a target of zero using a 20-second linear ramp command

issued in force control mode. This unloading step ends when the user selects a virtual button to manually end the test. Before the routine terminates, another short “dwell” command executes in displacement mode to switch the controller from force control to displacement control. This prevents unpredictable movement in the piston during specimen removal.

Chapter 3

Instrument Characterization and Calibration

Measurement of the elevated-temperature tensile testing instrument performance is necessary for conducting experiments under well-defined and repeatable conditions. For instance, controlling the temperature at the test specimen and determining the heat-up time requires an understanding of the split-tube furnace behavior. Additionally, determining how well specimens are protected from oxidation and how rapidly they are cooled requires tests to characterize the forming gas and air quenching systems, respectively. To measure the characteristics of the instrument and check that the design requirements described in Section 2.1 are met, physical tests were performed.

The instrument was tested to characterize the behavior of the split tube furnace, forming gas system, and air quenching system. A calibration curve relating the indicated furnace temperature to the temperature at the specimen gauge region was developed to enable accurate control of the specimen temperature. The recommended values for the forming gas flow rate and pressure for the air quenching system were determined and will be described. Preliminary tensile tests using Ti-IF steel specimens verified adequate oxidation protection of the specimen and confirmed the successful operation of the test frame control and data acquisition software. The methods for

characterizing the instrument and measuring its performance are described in the following sections.

3.1 Thermal Profiling

The temperature of the ATS 3210 split-tube furnace is controlled by an electronic proportional-integral-derivative (PID) controller. A K-type thermocouple integrated into the furnace provides the feedback signal for the PID controller. Because this furnace control thermocouple is located outside of the gas-tight retort, the temperature measured by the furnace controller does not accurately represent the specimen temperature. To control the temperature of the test specimen, a calibration curve relating the temperature from the control thermocouple to the specimen temperature is necessary. A calibration curve enables the controller reference temperature to be set to achieve a desired temperature at the specimen. The equilibrium temperature distribution along the vertical axis of the furnace is non-uniform. Quantifying this temperature variation is necessary to estimate the uncertainty in the specimen temperature. The process of measuring a calibration curve and the temperature distribution within the furnace is termed thermal profiling.

For thermal profiling, a dummy tensile specimen was installed with an Inconel-sheathed K-type thermocouple attached. The dummy specimen was cut from 0.003-inch thick nickel shim stock into a rectangle with the outer dimensions of the tensile specimen geometry (see Figure 2.1). Holes were punched in the ends of the dummy specimen to attach it to the tensile grips with pins. A small hole was punched in the center of the dummy specimen to attach the sheathed thermocouple. The thermo-

Table 3.1: Furnace Controller PID Values

Parameter	Value
Pr Band	85
Reset	0.10 min ⁻¹
Rate	1.20 min

couple wire was passed into the enclosure through the lower end of the fused-quartz tube. Two additional sheathed K-type thermocouples monitored temperatures near the centers of the top and bottom zones of the three-zone furnace. The spacing between each of the three thermocouples was approximately 4 inches. The rubber bellows at the bottom of the quartz tube was removed to accommodate the thermocouples. Consequently, the thermal profiling was conducted in air rather than in forming gas.

The furnace was thermally profiled at four temperatures: 750, 775, 800, and 825 °C. The power limiter knobs for the top, center, and bottom heating zones of the furnace were set to markings 5, 6, and 5 respectively. These settings for the three temperature zones were determined to provide a reasonably uniform temperature within the furnace. The values for the furnace PID controller are provided in Table 3.1. Temperatures were recorded once thermal equilibrium was reached at each of the four reference temperatures. Thermal equilibrium was assumed to be achieved when the temperature at each thermocouple remained constant to within one degree Celsius for a period of approximately five minutes.

Specimen thermocouple temperature was plotted against controller thermocouple temperature, and a least-squares linear regression was applied to obtain a

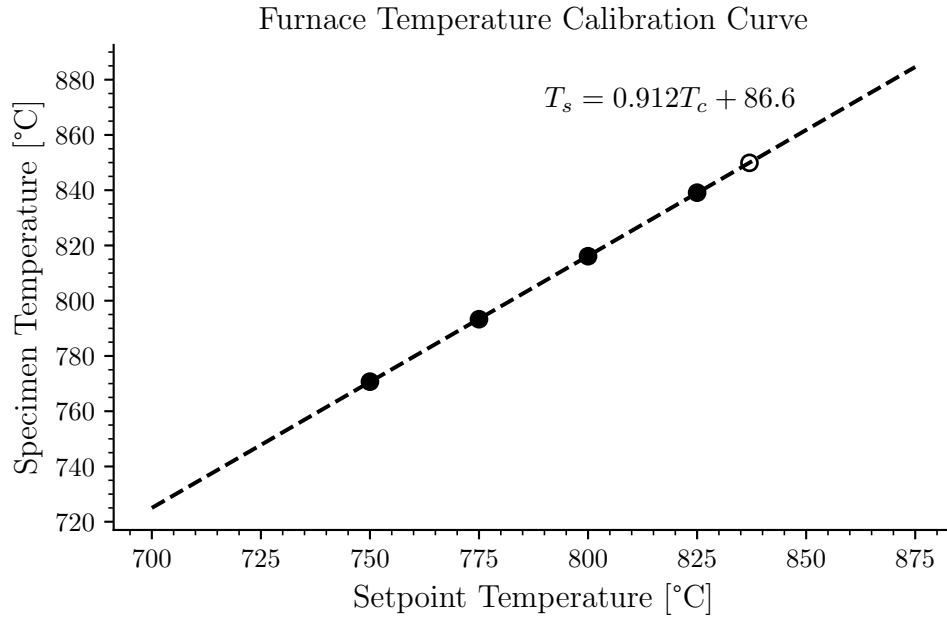


Figure 3.1: Specimen thermocouple temperature is plotted against the controller thermocouple temperature. The linear regression line and its corresponding equation are provided. The open circle indicates the measurement taken at a setpoint of 837 °C for verification.

calibration curve. To verify the calibration curve, the controller temperature was set to 837 °C, which corresponds to a projected specimen temperature of 850 °C, and the specimen thermocouple temperature was measured once thermal equilibrium was reached. The measured temperatures and the calibration curve are plotted in Figure 3.1. This plot provides the equation for the calibration curve, in which T_c and T_s refer to the controller temperature and the specimen temperature, respectively, measured in degrees Celsius. For a desired specimen temperature, the controller temperature is given by

$$T_c = 1.096T_s - 94.96. \quad (3.1)$$

The open circle shown in Figure 3.1 represents the measurement taken at a setpoint of 837 °C. The open circle falls very close to the linear regression line, indicating that the calibration curve may be extrapolated to slightly higher temperatures with good accuracy. The thermocouples in the top and bottom zones of the furnace read temperatures 15 and 33 °C cooler, respectively, than the center of the furnace.

3.2 Quench System Verification

To verify that the quenching system meets the design intent, the quench rate was measured. Like the thermal profiling procedure, a dummy specimen made from nickel shim stock was loaded into the grips, and a K-type thermocouple was attached at its center through a small hole. Unlike the thermal profiling procedure, the bellows was attached to the fused quartz tube because this is necessary for the quenching system to function. The specimen thermocouple was passed into the enclosure underneath the bellows connection at the lower stop. The seal around the thermocouple entry was checked prior to testing to ensure that the quench air would not leak out there. The specimen was heated to 850 °C, as measured by the specimen thermocouple. Once the specimen thermocouple reading stabilized, indicating that thermal equilibrium was reached, the quench air system was activated and the furnace was opened. The specimen temperature was logged as a function of time during the quenching process using a National Instruments USB-6210TM analog input device and LabVIEWTM software. Details regarding the LabVIEWTM program used to collect temperature measurements are given in Appendix D. The data logger and the quench air system were turned off once the specimen temperature reached

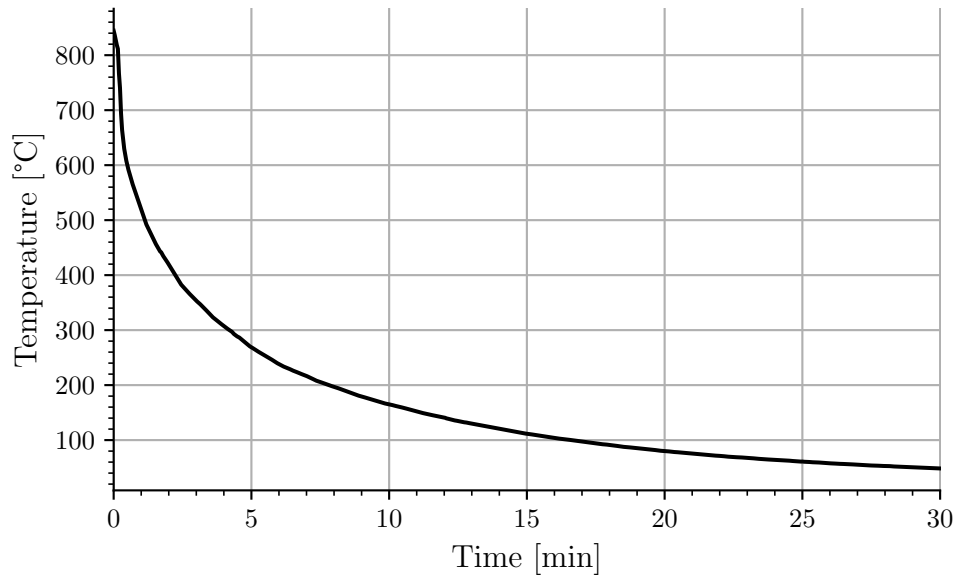


Figure 3.2: The dummy specimen temperature is plotted against time starting at the activation of the air quenching system. The initial specimen temperature was 850 °C.

approximately 50 °C.

The thermal properties of the dummy nickel specimen differ from those of the Ti-IF steel specimens intended for testing. However, because the specimen is small compared to the tensile grips, which act as large thermal masses, it is reasonable to assume that the difference in cooling rates between the nickel dummy specimen and Ti-IF steel specimens is negligibly small. The validation of this assumption is discussed later.

Figure 3.2 shows the dummy specimen temperature plotted against time starting from the initial activation of the air quenching system. At the onset of quenching, the temperature of the specimen dropped very rapidly. The specimen temperature

then approached room temperature as an approximately exponential decay, as expected for cooling dominated by forced convection.

The quenching process is intended to be rapid enough to preserve the subgrain microstructure present in the material during plastic deformation at elevated temperature. The preservation of subgrains is assisted by holding a constant tensile load during the quenching process. Because this application of load will cause continued creep deformation at high temperatures, the quenching system must be fast enough to prevent significant creep strain during quenching. To determine whether the quench air system preserves subgrain structure, it is ultimately necessary to image subgrains, or the lack thereof, in a specimen using a scanning electron microscope (SEM). This is discussed further in the next chapter. However, the performance of the quenching system is characterized here by calculating the time necessary to reduce the creep rate by a large factor, say 100. The time to reduce the creep rate depends on the material being tested, the dominant creep mechanism at the testing temperature, and the load applied. The primary intent of the high-temperature tensile instrument is to deform Ti-IF steels in uniaxial tension at relatively slow strain rates and temperatures near 850 °C. Thus, the approximate time required to reduce the creep rate of Ti-IF steel at 850 °C by a factor of 100 is considered as an appropriate performance metric for the quench system.

At a temperature of 850 °C and constant true-strain rate of 10^{-4} s^{-1} , Ti-IF steel undergoes steady-state dislocation-climb controlled creep, or five-power creep [6]. The phenomenological equation for steady-state five-power creep is [6]

$$\frac{d\varepsilon}{dt} = AD \left(\frac{\sigma}{E} \right)^n, \quad (3.2)$$

where D is the lattice self-diffusivity, σ is the true flow stress, E is the temperature-dependent unrelaxed dynamic elastic modulus, A is a material constant, and $n \approx 5$ is the stress exponent. During the quenching process, the load on the test specimen is held constant. This provides a nearly constant σ if strain accumulation during quenching is small. Assuming that E does not change appreciably with temperature, Equation 3.2 may be simplified to

$$\frac{d\varepsilon}{dt} \propto D. \quad (3.3)$$

The validity of the assumption that E is constant is discussed later. From this relation, it is clear that the creep rate will decrease by a factor of 100 when the lattice self-diffusivity reduces by a factor of 100. It is assumed that another creep mechanism does not begin to dominate as the temperature drops. The lattice self-diffusivity data for pure Fe from Oikawa [15] indicate that D decreases by a factor of 100 as T drops from 850 °C to 727 °C. The diffusivity data for Fe are representative of Ti-IF steels because small alloying additions do not appreciably affect the lattice self-diffusivity [15]. Referring to Figure 3.2, the specimen temperature reduces from 850 °C to 727 °C after 16 seconds of quenching. This is about one order of magnitude faster than the cooling rate achieved between the same temperatures from previous experiments, performed by the author, in the vacuum furnace instrument.

It should be noted that the temperature-dependent elastic modulus does not change significantly between these temperatures, according to data for Fe by Köster [16]. In fact, as the temperature reduces, the elastic modulus slightly increases. This makes the preceding analysis conservative because the increase in elastic modulus

with decreasing temperature causes the creep rate to drop even more rapidly than if the elastic modulus remained constant.

3.3 Performance in a Demonstration Tensile Test

A demonstration tensile test was performed to check the operation of the elevated-temperature tensile testing instrument and the control software. The test was conducted using a Ti-IF steel specimen with the rolling direction oriented parallel to the tensile axis. The specimen was strained at a constant true-strain rate of 10^{-4} s^{-1} to a final true strain of 0.1 at a temperature of 850 °C. The forming gas flow rate was adjusted to achieve good oxidation protection. More details regarding the tensile testing procedure are provided in the next chapter.

The test specimen showed insignificant amounts of oxidation following testing and quenching. It was determined that a forming gas flow rate of 96 cm³/min (indicated by the 10 mm mark on the flow meter) is sufficient to prevent significant oxidation of the specimen at 850 °C. The flow meter scale is shown in Figure 2.7. During the first 30 minutes of heat up, set the flow rate to 260 cm³/min (indicated by the 20 mm mark) to ensure that the air in the retort is fully displaced by forming gas before elevated-temperatures are reached. Appendix E provides flow rates for nitrogen corresponding to marker locations on the flow meter scale.

Chapter 4

Elevated-temperature Tensile Tests of Ti-IF Steel

To confirm the functionality of the instrument, Ti-IF steel tensile specimens were tested in tension to predetermined true strains at a constant true-strain rate and elevated temperature. The true strain rate was 10^{-4} s^{-1} , and the test temperature was $850 \text{ }^\circ\text{C}$ for all tests. Six tension tests were performed to the targeted true strains listed in Table 4.1, which also lists the actual strain achieved by each test.

For the sixth test, a K-type thermocouple was spot welded to the gauge region of the specimen to measure specimen temperature during the test, including quenching. Tested specimens were sectioned, mounted, and polished for metallography. A scanning electron microscope (SEM) was used to observe specimen microstructures. Grain size measurements were obtained from SEM photomicrographs using the lineal intercept method as defined in ASTM E112-13 [17].

Table 4.1: Targeted and Actual True Strains for Tests Performed

Test Number	Target True Strain [-]	Actual True Strain [-]
1	0.100	0.113
2	0.100	0.076
3	0.100	0.086
4	0.120	0.101
5	0.140	0.124
6	0.095	0.84

The Ti-IF steel sheet material was provided by I/N Tek (New Carlisle, IN). The material composition reported by the supplier is listed in Table 4.2. The nominal sheet thickness is 0.69 mm (0.0272 in).

Table 4.2: The composition of the Ti-IF steel sheet, as provided by the supplier, is listed in weight percent.

Mn	Al	Ti	Cr	Cu	Ni	S	P	Nb	Si	Mo
0.1319	0.065	0.0428	0.0294	0.0188	0.0185	0.0118	0.0112	0.0097	0.0049	0.004
As	N	C	Pb	Sn	V	Sb	B	Ca	Fe	
0.0034	0.00248	0.0024	0.001	0.001	0.001	0.0007	0.0001	0.0001	bal.	

4.1 Experimental Procedures

4.1.1 Tensile Specimen Preparation

Tensile specimens were excised from a single Ti-IF steel sheet by water-jet cutting. Specimens were produced with three different tensile axis orientations: parallel, perpendicular, and 45° to the sheet rolling direction (RD). Only specimens with the tensile axis parallel to the sheet RD were tested. Other specimen orientations were reserved for future testing. A technical drawing of the tensile specimen geometry is shown in Figure 2.1. A unique specimen identifier was engraved in the grip regions at both ends of every specimen. The edges of the gauge region and the pin holes were de-burred to remove rough features. This facilitated pin insertion during specimen installation and increased the geometric uniformity of the gauge region.

The dimensions of the gauge region were measured for each specimen prior to testing. The gauge width and thickness were averaged over three measurements. Because fillets are present on the ends of the gauge length, the gauge length cannot

be directly measured. The gauge length was estimated by measuring the distance between the opposing grip region faces and subtracting twice the nominal fillet radius. The gauge length was averaged over two measurements, one on each side of the gauge region.

The front and back faces of each tensile specimen were imaged using a document scanner at 600 dpi before and after testing. A 0.5-inch steel gauge block was included in each scan as a length reference. These images provide quantitative documentation of the specimen geometry.

4.1.2 Elevated-temperature Tensile Testing

The following procedure was defined and used for all tests. Before installing a specimen to test, do the following in order. First, turn on the pressure to the air quenching system and to the forming gas system. Power on the MTS FlexTest 40TM digital controller and the hydraulic power unit for the MTS 810 test frame. Next, open the valves for the recirculating chilled water system to provide cooling for the hydraulic pump and the test fixtures. Start the MTS Station ManagerTM and MPE software programs on the control computer. Follow the standard operating procedure document located at the control computer for MTS system operation. Using the Station ManagerTM software, move the piston to the approximate location for specimen installation and offset the piston displacement and load readings to zero. In the same software, set the system limits to piston displacements of ± 0.5 inches and forces of ± 1.8 kip from the zeroed values. For safety, the control software depressurizes the test frame hydraulics if these limits are exceeded.

To install a test specimen, do the following. First, coat the pins with boron nitride paint to prevent seizure and facilitate specimen removal following testing. Next, detach the bellows connection at the bottom of the retort. While lifting the retort, attach the specimen to the upper tensile grip with a pin. Offset the load value to zero again. Using the Station ManagerTM software, incrementally adjust the position of the lower tensile grip until the lower pin can be easily inserted. The load reading should not change from zero after installing the specimen and lowering the retort. If the load does change, repeat the specimen installation.

With the specimen installed, do the following. Reattach the bellows to seal the fused quartz tube. Check the bellows seal for leaks by temporarily pressurizing the quench air system. Once the seal is checked, offset the load value to zero a final time to remove any load reading from the attached bellows on the system. Start the test routine in the MPE software to remove slack in the load train and place a load of 1 lbf on the specimen for heat-up. When prompted by the software, enter the displacement for the desired final true strain. To determine the final displacement, first calculate the specimen gauge length, L_T , at the test temperature, T , using the following equation:

$$L_T = L_0 [1 + \alpha(T - T_0)]. \quad (4.1)$$

In Equation 4.1, T_0 is room-temperature, L_0 is the room-temperature gauge length, and α is the linear thermal expansion coefficient. For Ti-IF steel, $\alpha = 1.17 \times 10^{-5} \text{ }^\circ\text{C}^{-1}$ [5]. Calculate the final displacement, u_f , according to

$$u_f = L_T (e^{\epsilon_f} - 1), \quad (4.2)$$

where ε_f is the desired final true strain.

Close the split tube furnace and power on the furnace controller. Set the controller temperature to 837 °C, which will produce a specimen temperature of 850 °C, and start the automatic temperature control. Use the power limiter settings and tuning parameters described in Section 3.1.

Shortly after starting the ramp to the testing temperature, start the forming gas flow by slowly opening the valve on the adjustable flow meter. Adjust the flow of the forming gas until the flow meter ball reaches the 20 mm marking. After the first 30 minutes of heating, reduce the flow of the forming gas until the ball reaches the 10 mm marking. The flow of forming gas may be started after the furnace because the furnace ramps to the testing temperature relatively slowly. The furnace typically reaches the set-point temperature within 30 minutes.

Start the deformation step in the MPE software 1 hour after reaching the test temperature. This allows the specimen to recrystallize and the pull-rods to complete thermal expansion. The specimen is strained at a constant true-strain rate until the prescribed final displacement is reached. Then, the software automatically switches to force control mode and maintains a constant load on the specimen.

Once the final displacement is reached, perform the following actions quickly and in the order presented. For safety, wear a lab coat and face shield. Close the valve on the adjustable flow meter to stop the forming gas flow. Switch the furnace controller to “stop.” Note that the furnace controller should not be powered off. Activate the air quenching system and, using high-temperature gloves, open the furnace.

Wait at least 30 minutes before stopping the air quench. After cooling to room temperature, stop the control software, save the mechanical test data, and remove the specimen from the grips.

4.1.2.1 Mechanical Data Processing

The MPE software exports time, load, and piston displacement data. These data were processed using two Python scripts. The first script removes the data from heat-up and quenching. The second script applies corrections to the data and plots the true stress against true strain. The displacement data are shifted so the elastic region of the load-displacement curve passes through the origin. A second-order Butterworth low-pass filter with a cutoff frequency of 0.25 Hz removes noise from the load and displacement data. These Python scripts are provided in Appendix C.

4.1.2.2 Tensile Testing with Temperature Monitoring

The specimen temperature was monitored during the sixth tensile test using a K-type thermocouple welded to the specimen. In addition to the preparation described in Section 4.1.1, the specimen gauge region was lightly sanded using 600 grit paper. This removed oxidation and improved the thermocouple weld. The thermocouple junction was formed between 0.010-inch diameter chromel and alumel wires using a DCC Hotspot ITM spot welder. The thermocouple junction was spot welded to the center of the specimen gauge region. Ceramic thermocouple insulators were installed over the thermocouple wires to prevent short-circuiting. Figure 4.1 shows

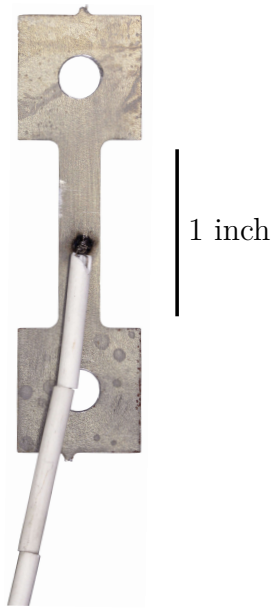


Figure 4.1: This photograph shows the thermocouple attached to the specimen gauge region for the sixth tensile test.

the thermocouple attached to the specimen.

The specimen was installed as described in Section 4.1.2. The thermocouple wire was passed through the lower seal. This seal was checked for air leakage prior to testing. Specimen temperature was monitored for the entire test duration, including heat-up and quenching, using the hardware and LabVIEWTM program described in Section 3.2. The testing procedure was otherwise identical to that described in Section 4.1.2.

4.1.3 Metallographic Sample Preparation

Tensile specimens were sectioned for metallography using an Allied High Tech TechCut 4TM diamond saw. As shown in Figure 4.2a, three pieces were excised from

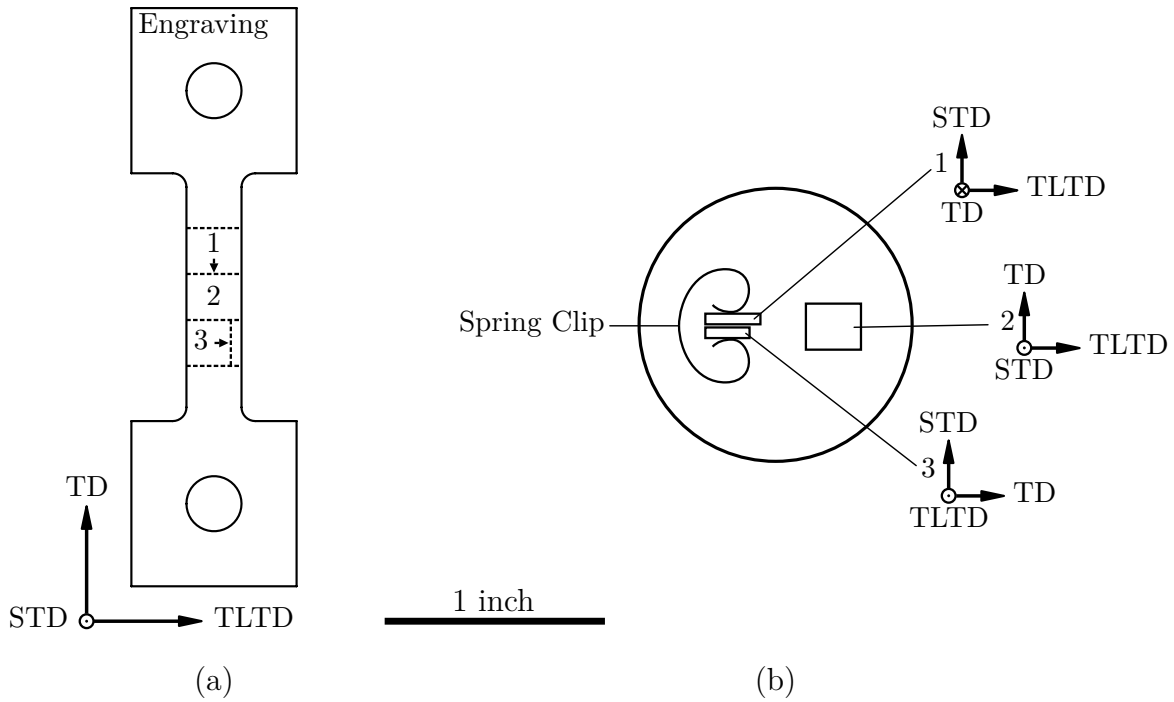


Figure 4.2: (a) The dashed lines in the schematic indicate how each tensile specimen was sectioned for metallography. The arrows on sections 1 and 3 indicate the surfaces visible in the mount. (b) This schematic depicts the layout and orientation of each sectioned piece in a single mount. Note that “•” and “×” represent arrows out of and into the page respectively.

each specimen to view specimen plane sections normal to the tensile direction (TD), tensile long transverse direction (TLTD), and short transverse direction (STD). For each tensile specimen, these three pieces were compression molded into 1.25-inch diameter mounts using Buehler ProbeMet™ conductive molding compound. The layout of the sections for mounting is shown schematically in Figure 4.2b.

The metallographic specimens were ground and polished for scanning electron microscopy using an Allied High Tech E-Prep 4™ automatic polishing machine. Ta-

ble 4.3 provides procedures for grinding and polishing. Note that the times listed are minimum times spent on each step. The first grinding step was performed until 200 μm of material was removed. The last polishing steps from 3 μm diamond suspension to colloidal silica were repeated as necessary to obtain clear backscattered electron images. The specimens and polishing machine were cleaned thoroughly between each step to prevent cross-contamination of polishing media.

Table 4.3: The grinding and polishing steps used to prepare Ti-IF steel specimens for metallography are listed.

Polishing Surface	Polishing Media	Lubricant	Platen Speed [RPM]	Head Speed [RPM]	Force [N]	Time [min]
1200 grit SiC	-	Water	300	100	20	Until Planar
Leco Pan-W	9 μm Diamond Suspension	Aqua Lube	150	50	5	15
Leco LeCloth	3 μm Diamond Suspension	Aqua Lube	150	50	5	25
Leco LeCloth	1 μm Diamond Suspension	Aqua Lube	150	50	5	30
Leco Imperial	Colloidal Silica	Deionized Water	150	50	5	60

4.1.4 Scanning Electron Microscopy

Photomicrographs were taken using a TESCAN VEGA3 SEM equipped with a backscattered electron (BSE) detector. The BSE detector provides electron channeling contrast between grains of different crystallographic orientation. A short working distance, a high beam current, and a large spot size produce the clearest SEM-BSE images at low magnification. SEM-BSE images were taken with a working distance of 15 mm, an accelerating voltage of 10 kV, and a beam intensity of 16. For the working distance and accelerating voltage stated, this beam intensity corresponds to a beam current of 1.4 nA, measured through the specimen, and a spot size of 390 nm. The magnification for SEM-BSE imaging ranged from $200\times$ to $2000\times$.

Grain size measurements were obtained from low magnification SEM-BSE photomicrographs using the lineal intercept method defined in ASTM E112-13 [17]. Grain sizes can be measured in metallographic views normal to the TD, STD, and TLTD. Grain size was measured in the TD-TLTD plane (orientation 2 in Figure 4.2) at magnifications of $200\times$ and $500\times$.

4.2 Experimental Results and Discussion

4.2.1 Mechanical Testing

To check the strain control performance of the instrument, the targeted specimen true strain and independently measured specimen final true strain are compared. The targeted and measured true strains for all tests are provided in Table 4.1. In all tests except the first, the measured true strains were less than the targeted values by 15% on average. The quenching system rapidly cools the specimen below the tem-

perature regime for creep to halt plastic deformation. Thus, the start of quenching affects the true strain achieved. Because the operator activates the quench system, some operator-induced error is expected in the final true strains. A comparison of the maximum piston displacements with the target values provides a better estimate of this error. The maximum displacement from each test, excluding the first, was larger than the target value by less than 2%. This suggests that errors from manual quench activation do not fully account for the differences between the targeted and measured true strains. However, these data demonstrate that an operator can control the final displacement with reasonable precision for a slow constant true-strain rate of 10^{-4} s^{-1} .

The measured true strain in the first test was higher than intended for two reasons. First, delayed quenching enabled continued plastic straining at the beginning of cool-down. Second, a tensile load of 5 lbf was applied to the specimen during heat-up. This likely produced significant creep strain during the one-hour thermal soaking period. The tensile load for heat-up was reduced to 1 lbf for subsequent tests. Data from the first tensile test are excluded from the remaining analyses.

Grip region deformation accounts for the remaining differences between the targeted and measured final true strains. The most significant grip region deformation is pin-hole elongation, which causes the final true strain within the gauge length to be less than the target value. Figure 4.3 shows representative scanned images of a specimen before and after testing. Pin-hole elongation is apparent in the post-test specimen image. Measurements of the pin-hole elongation were made from scanned specimen images. On average, pin-hole elongation accounted for 20% of the final

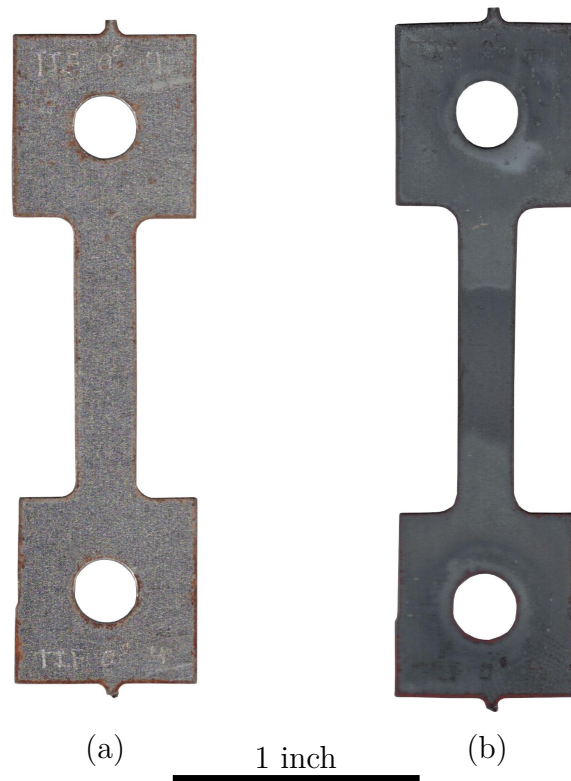


Figure 4.3: Scanned images of a specimen are shown (a) before and (b) after testing. Pin-hole elongation is apparent in the upper grip region of the tested specimen. The darkened region at the center of the gauge region in (b) is from modest oxidation by the pressurized air used for quenching.

true strain measured from the piston displacement. Including the manual quenching error, this completely accounts for the observed differences between the targeted and measured true strains. Thus, the measured true strains are lower than the targeted values primarily because of pin-hole elongation. Normal variations in quench activation produce smaller errors in the final true strains.

The true-strain rate achieved was calculated using the final true strain measured from the specimen gauge region. The true-strain rate, averaged over all tests,

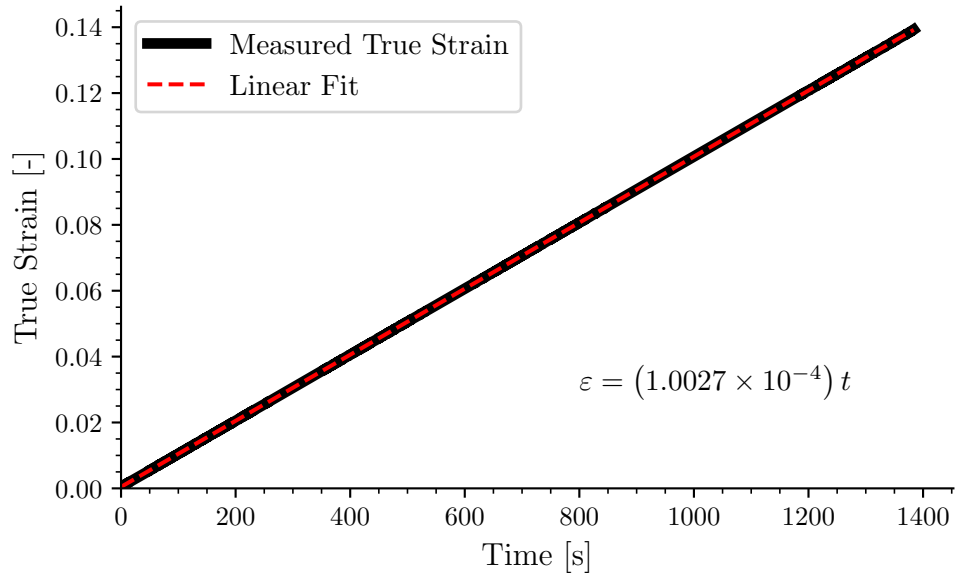


Figure 4.4: True strain data from the fifth tensile test are plotted as a function of time. A linear regression line is also plotted.

was $8.5 \times 10^{-5} \text{ s}^{-1}$, which is lower than the target true-strain rate of 10^{-4} s^{-1} by 15%. The error in the true-strain rate achieved is also caused by pin-hole elongation. To verify the control of the test frame piston motion, the true-strain rate was calculated from displacement data. Figure 4.4 presents true strain, calculated from displacement data, plotted against time from one test. The slope of these data, calculated by linear regression, is the average true-strain rate. The average true-strain rates were within 0.5% of the target value of 10^{-4} s^{-1} . The coefficient of determination from linear regression, denoted R^2 , was greater than or equal to 0.9999987 for each test. This indicates very good agreement between the data and regression line. These true-strain rate data support two conclusions. First, the implemented displacement control method produces an average true-strain rate very close to the intended value,

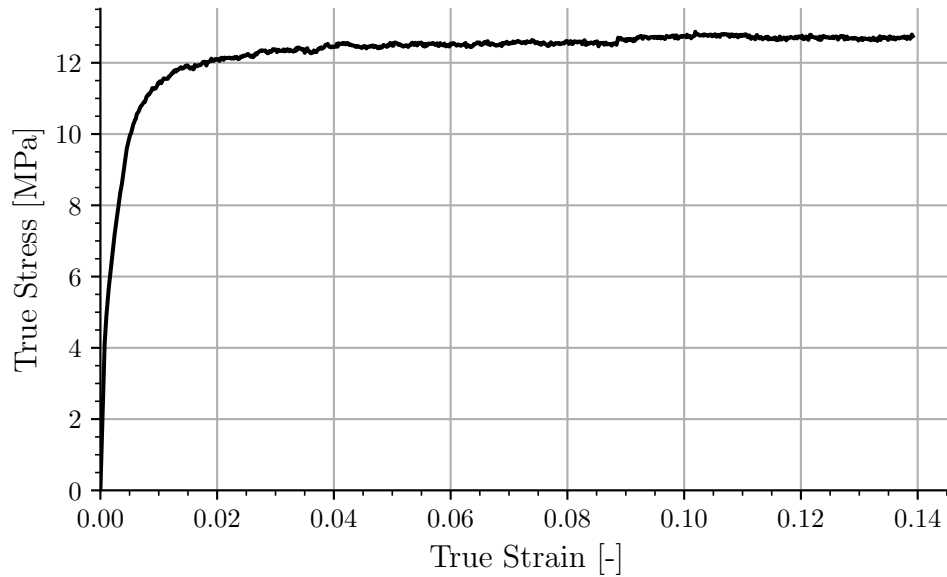


Figure 4.5: True stress and true strain data from the fifth tensile test are plotted. The flow stress behavior shown is representative of that observed in all other tests.

assuming there is no grip region deformation. Second, the proximity of the R^2 values to unity implies that the actual piston motion does not significantly deviate from its intended motion.

Figure 4.5 presents true stress plotted against true strain for the fifth test. The data from this test are representative of the other tests performed. The relatively constant flow stress observed in the plastic region is indicative of steady-state creep behavior. The flow stress averaged over all tests was 11.4 MPa with a standard deviation of 0.9 MPa. The flow stresses observed agree closely with those from previous tests performed under vacuum for the same material, test temperature, and true-strain rate; see Ref. [6, 7].

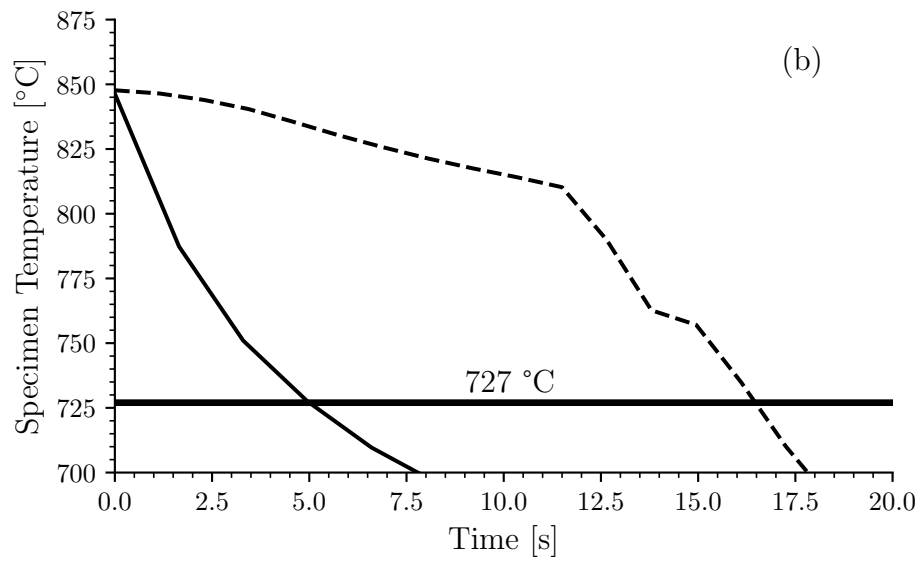
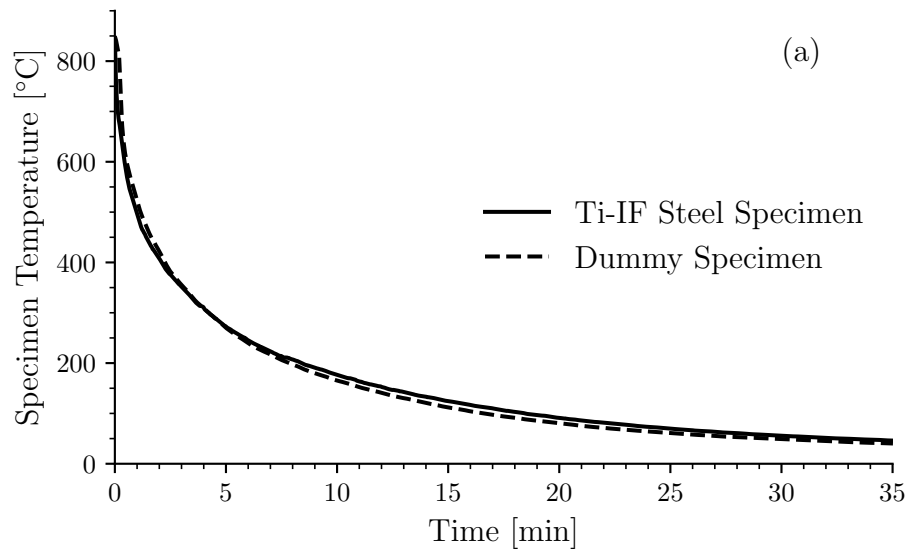


Figure 4.6: (a) The measured specimen temperatures are plotted against quenching time. (b) The first 20 seconds of quenching shows the initial temperature drop. The line at 727 °C indicates where the creep rate would decrease by a factor of 100, as calculated in Section 3.2. The legend applies to both plots.

The temperature of the specimen gauge region was monitored with a thermocouple welded to the specimen during the sixth test. From the time the test temperature was reached until the start of quenching, the average measured specimen temperature was 846 °C. During this period, the temperature fluctuated by less than 2 °C. The maximum deviation from the intended specimen temperature of 850 °C was 5 °C. This demonstrates that the furnace can control the specimen temperature closely to the intended test temperature and maintain this temperature during tensile deformation. If the set temperature of the controller were further adjusted, the temperature could be controlled to $850\text{ °C} \pm 2\text{ °C}$.

The specimen temperature in the sixth tensile test is plotted against the time from the start of quenching in Figure 4.6. Also plotted are temperature data obtained using the dummy specimen, described in Section 3.2. During quenching, the specimen temperature decreased at a rate similar to that of the dummy specimen. The initial quench rate measured with the welded thermocouple was higher than that of the dummy specimen. In Section 3.2, the time to reduce the creep rate by a factor of 100 during quenching was used as a performance metric. This was shown to be the time to reduce the specimen temperature from 850 °C to 727 °C. For the Ti-IF steel specimen, this time was approximately 5 seconds, whereas for the dummy specimen it was 16 seconds. The times for the Ti-IF steel specimen and dummy specimen to cool to room temperature were similar. The close agreement between the two measurements suggests that the methods described in Chapter 3 are sufficient for thermal profiling and quench rate measurement. The thermocouple-welded specimen oxidized significantly more than the other specimens tested. Air leakage into the

retort through the thermocouple wire pass-through is likely the cause of this oxidation. Because of this, direct temperature monitoring using a welded thermocouple is not recommended for future testing.

4.2.2 Metallography

Figures 4.7 and 4.8 are BSE photomicrographs from the TD-TLTD plane at magnifications of $200\times$ and $1000\times$, respectively, of the third test specimen. The microstructure contains uniformly equiaxed grains, which is consistent with recrystallization and normal grain growth. Subgrain structures are apparent in several large grains. Similar microstructures were observed in the other tested specimens. The appearance of subgrains is consistent with water-quenched Ti-IF steel specimens from a previous study [2]. This demonstrates that the air quenching system preserves microstructures developed during deformation at elevated temperatures. Thus, the quench rates determined in Sections 3.2 and 4.2.1 are reasonable for preserving microstructures.

Lineal intercept grain sizes were measured for each specimen tested. To compare deformed and undeformed microstructures, the lineal intercept grain size was measured for a specimen statically annealed at $850\text{ }^{\circ}\text{C}$ for 77 minutes. This time is equivalent to the time-at-temperature for specimens strained to 0.1 true strain. Grain sizes are plotted against measured true strain in Figure 4.9. The mean recrystallized grain size, measured from the statically annealed specimen, is plotted for comparison. The grain sizes of the deformed specimens are larger than the grain size after static annealing.

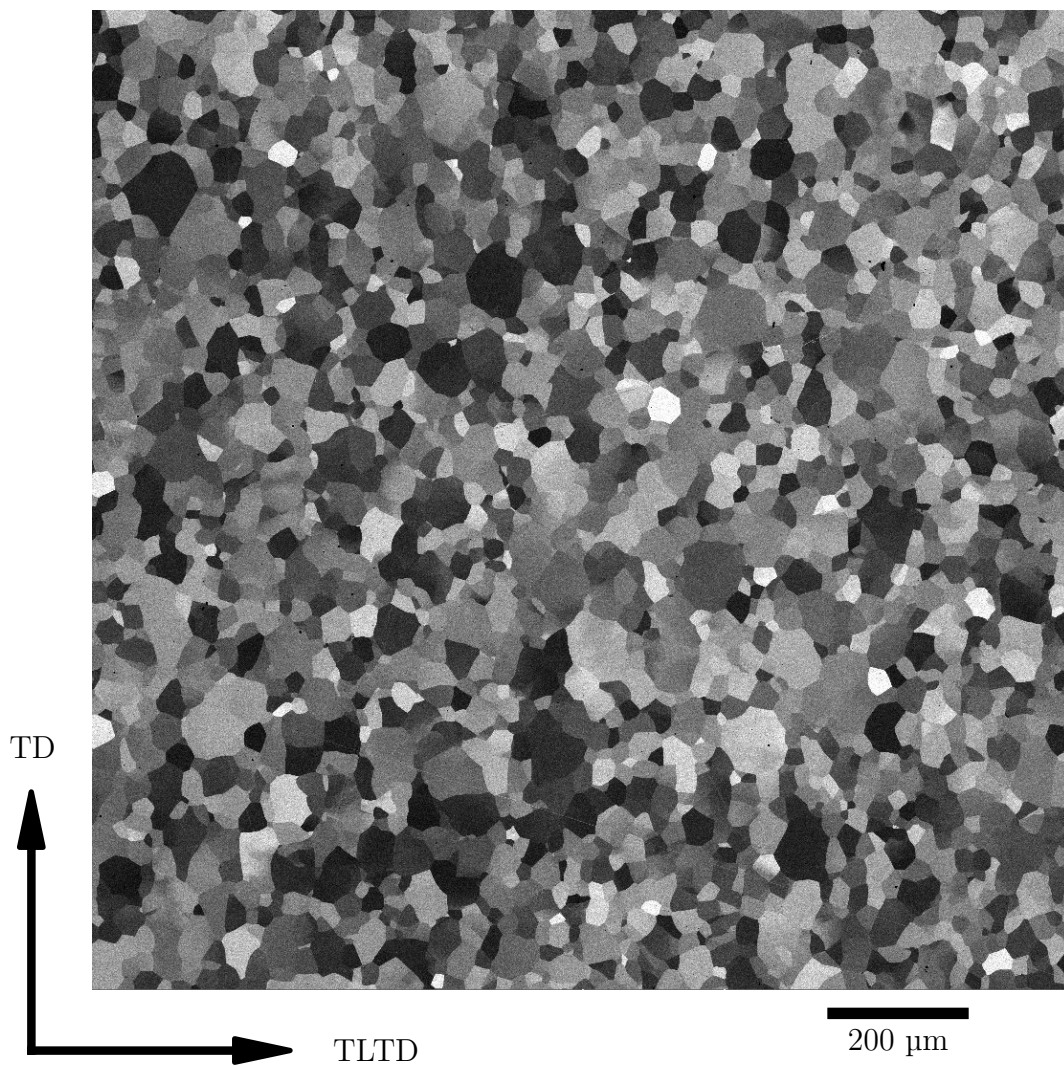


Figure 4.7: This BSE photomicrograph shows the microstructure in the TD-TLTD plane of the third specimen tested. The microstructure shown is representative of all specimens tested in tension.

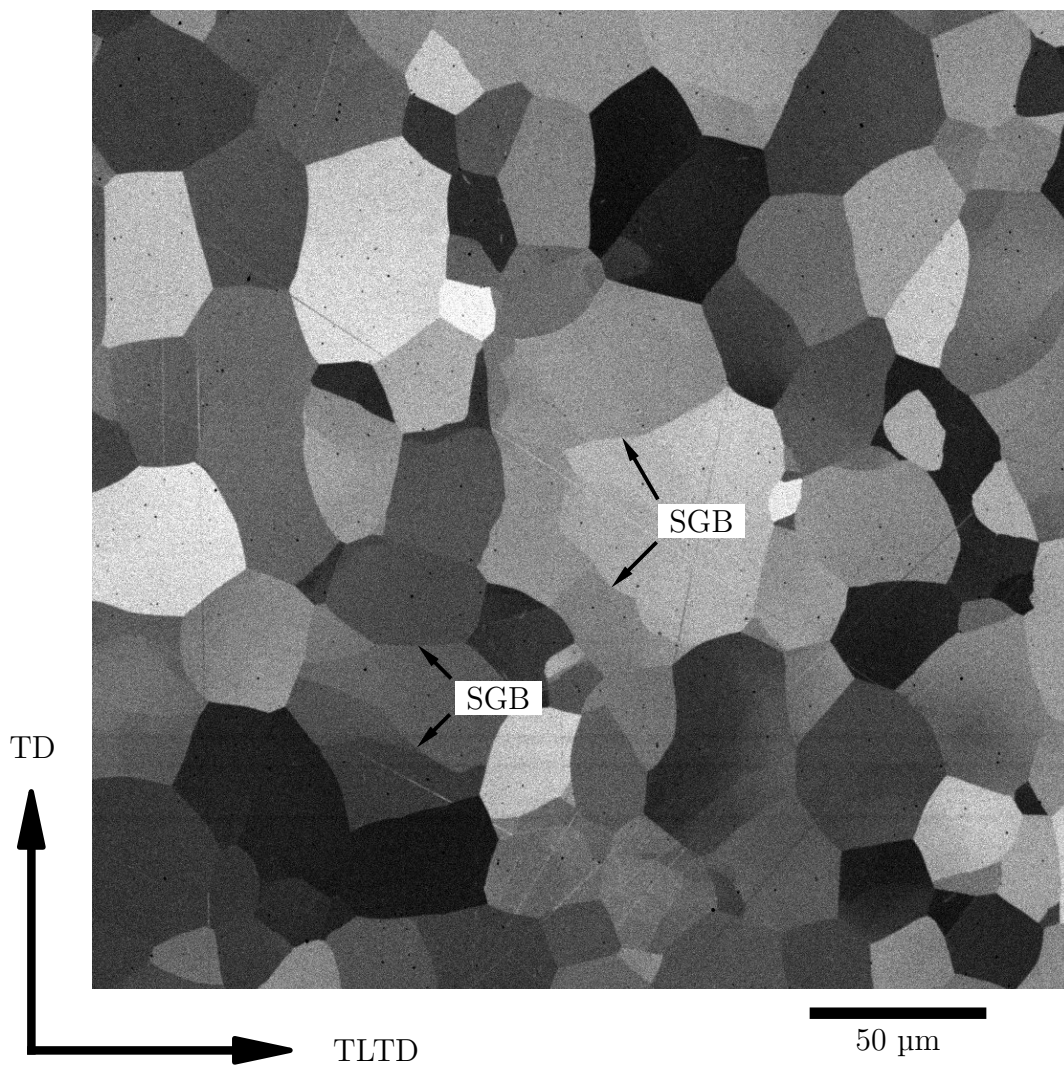


Figure 4.8: This BSE photomicrograph, taken in the TD-TLTD plane, shows apparent subgrains in the microstructure of the third specimen tested. Examples of apparent subgrain boundaries are labeled as “SGB.”

The mean grain sizes measured in deformed specimens at $200\times$ magnification range from 31 to 37 μm , while the mean grain size of the statically annealed specimen is $26.0 \pm 1.7 \mu\text{m}$. From measurements at $500\times$, deformed specimen grain sizes range from 27 to 32 μm and the statically annealed specimen grain size is $20.6 \pm 3.8 \mu\text{m}$. This indicates that deformation at elevated temperature produces a faster grain growth rate than does static annealing; dynamic grain growth is faster than static grain growth. Similar behavior was documented in studies where DNGG was observed in the same material [2, 6]. Figures 4.9a and 4.9b show that grain size does not significantly change with increasing final true strain. This is inconsistent with previous observations that grain size increases with true strain [2, 6]. However, the range of final true strains investigated was narrow compared to those previously studied. It is likely that, for the narrow range of final true strains investigated, the lineal intercept method for measuring grain size was not sensitive enough to detect the grain size changes observed in previous studies.

The differences between the grain sizes measured at $200\times$ and $500\times$ magnification are approximately within the error bars of the grain size data. However, the mean grain sizes measured at $500\times$ are slightly lower than those measured at $200\times$. This is likely because grain boundary intercepts are more easily identified at higher magnifications. An increase in the number of grain boundary intercepts counted decreases the measured average grain size. The grain size error bars tended to be larger for the measurements taken at $500\times$. This is expected because fewer grains are sampled at higher magnification compared to lower magnification.

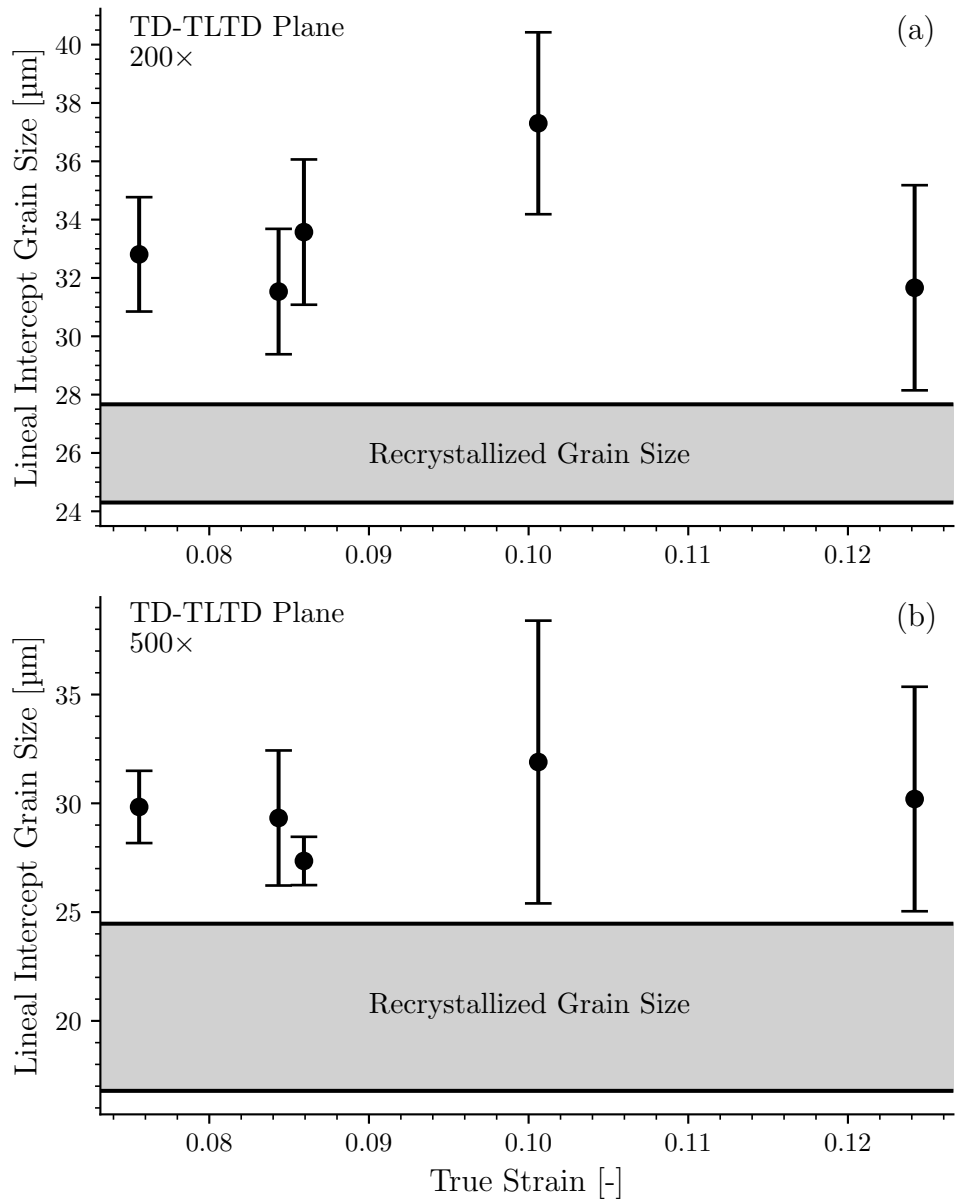


Figure 4.9: Lineal intercept grain sizes are plotted against true strain. The grain size measurements are from photomicrographs of the TD-TLTD plane taken at (a) 200× and (b) 500×. The recrystallized grain size is indicated by the shaded region. The error bars and the shaded region represent the 95% confidence intervals of the measurements.

Chapter 5

Conclusions and Future Work

5.1 Conclusions

An elevated-temperature tensile testing instrument was designed and constructed for investigating DGG phenomena in a Ti-IF steel. The instrument deforms a test specimen in uniaxial tension at elevated temperature in a reducing environment and subsequently quenches that specimen while maintaining an applied tensile load. The reducing environment prevents significant oxidation at elevated temperatures. Rapid specimen quenching under an applied tensile load preserves the microstructure produced by elevated-temperature deformation. This is confirmed by subgrain boundaries visible in SEM-BSE photomicrographs of tested specimens. The capability to deform a specimen at elevated temperature without significant oxidation and preserve the resulting microstructure is unique to this instrument and facilitates the study of DGG phenomena.

DNGG was observed in Ti-IF steel specimens tested in tension at a constant true-strain rate of 10^{-4} s^{-1} and temperature of 850 °C. Under these tensile testing conditions, a nearly constant flow stress of $11 \pm 1 \text{ MPa}$ was observed. These results agree with those for the same material previously tested under vacuum [6, 7]. Lineal intercept grain size measurements show that DNGG is more rapid than SNGG. This

also agrees with previous work on the same material [2, 6]. The successful operation of the instrument and replication of previous results confirms that it provides the capabilities needed to further investigate DGG phenomena.

5.2 Suggestions for Future Work

The author recommends utilizing the elevated-temperature tensile testing instrument developed in the present work for investigating DGG in IF steels and other materials susceptible to oxidation. Mechanisms for DGG should be identified and interrogated. The effects of the following variables on microstructure evolution during DGG should be probed:

- Specimen temperature
- True-strain rate
- Final true strain
- Tensile direction orientation relative to the rolling direction

The author suggests electron backscatter diffraction (EBSD) for microstructure characterization. EBSD data may be readily processed to measure distributions of grain size and orientation. High-resolution electron backscatter diffraction (HR-EBSD) is specifically recommended because the high angular resolution enables more reliable detection of low-angle boundaries for the identification of subgrains.

The final true strains and true-strain rates achieved were, on average, 15% lower than the target values because of pin-hole elongation. The author recommends

mitigating pin-hole elongation effects in future elevated-temperature tensile tests. Shoulder-loading tensile grips are expected to produce less grip region deformation than pin-loading grips. Reducing grip region deformation should improve the control of final true strain and true-strain rate.

Appendices

Appendix A
Technical Drawings

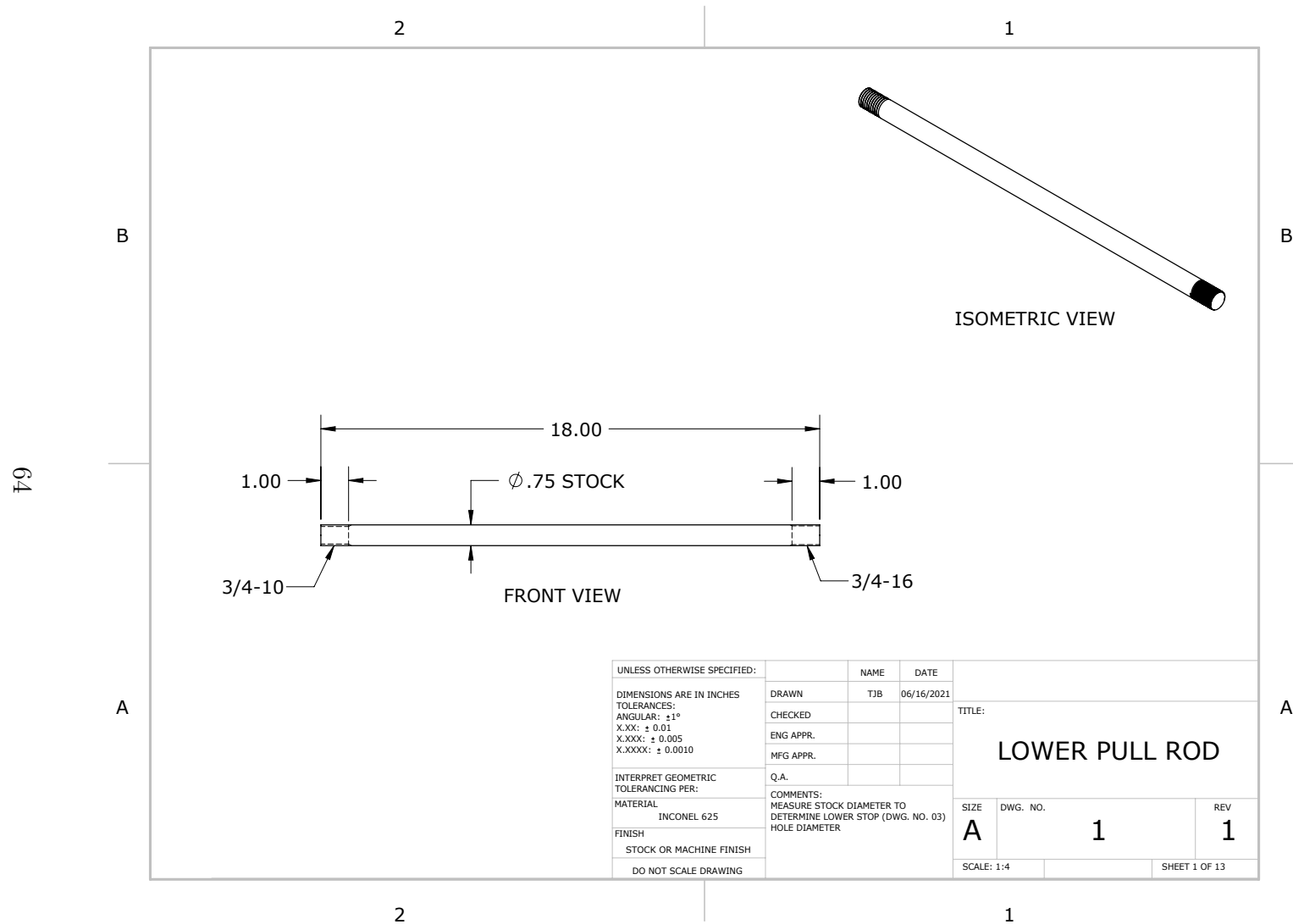


Figure A.1: Shown is the technical drawing for the lower pull-rod.

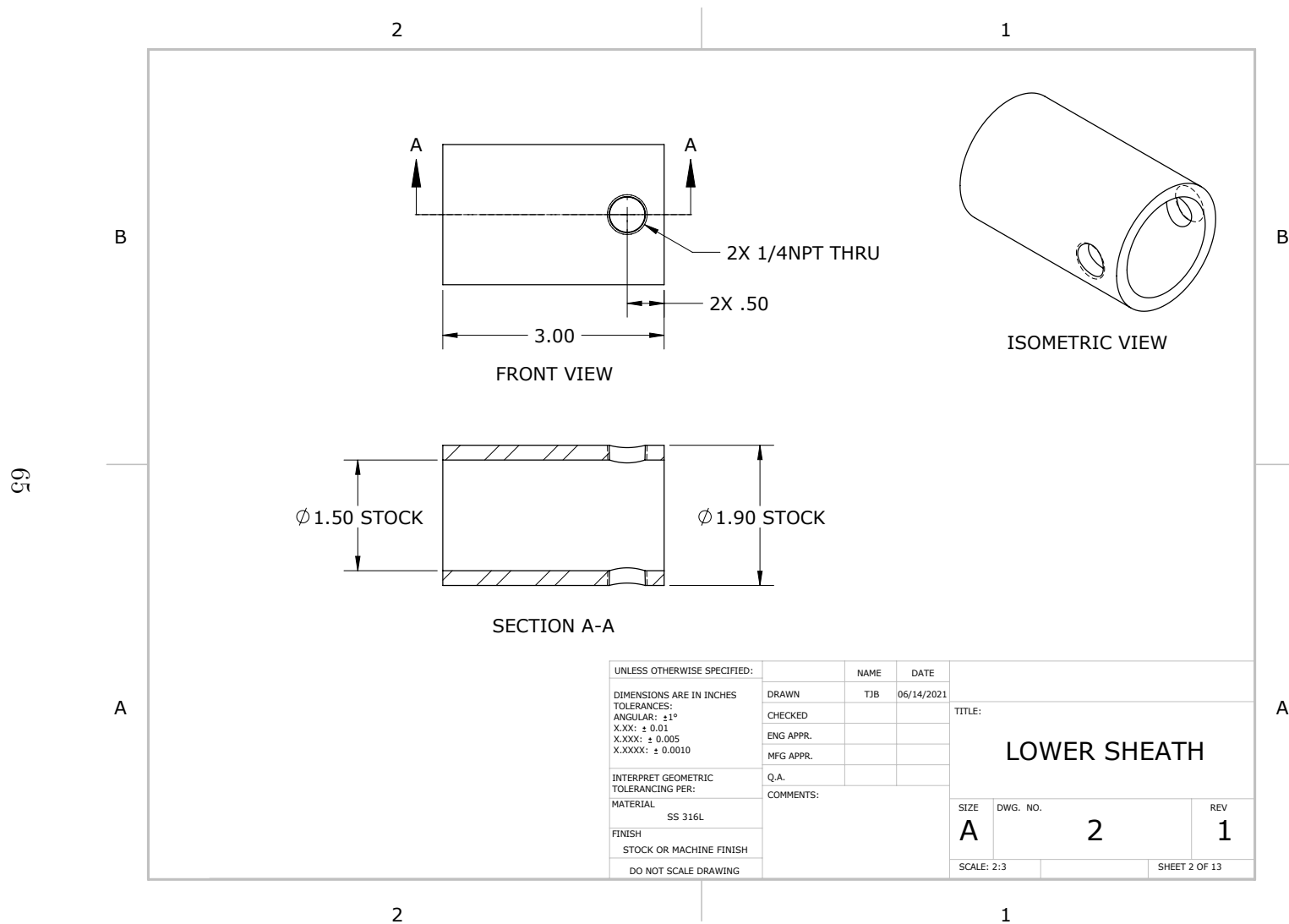


Figure A.2: Shown is the technical drawing for the lower sheath.

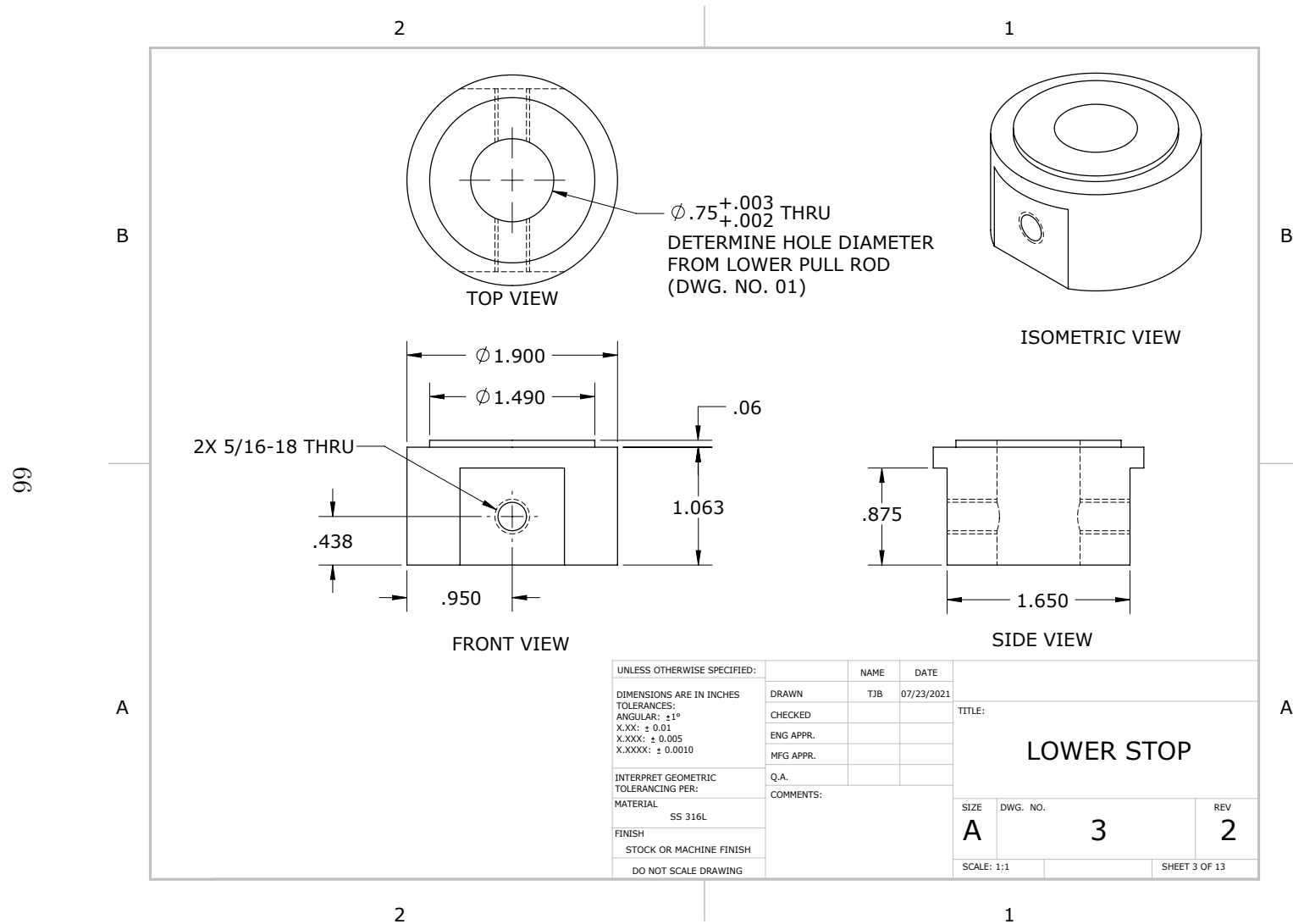


Figure A.3: Shown is the technical drawing for the lower stop.

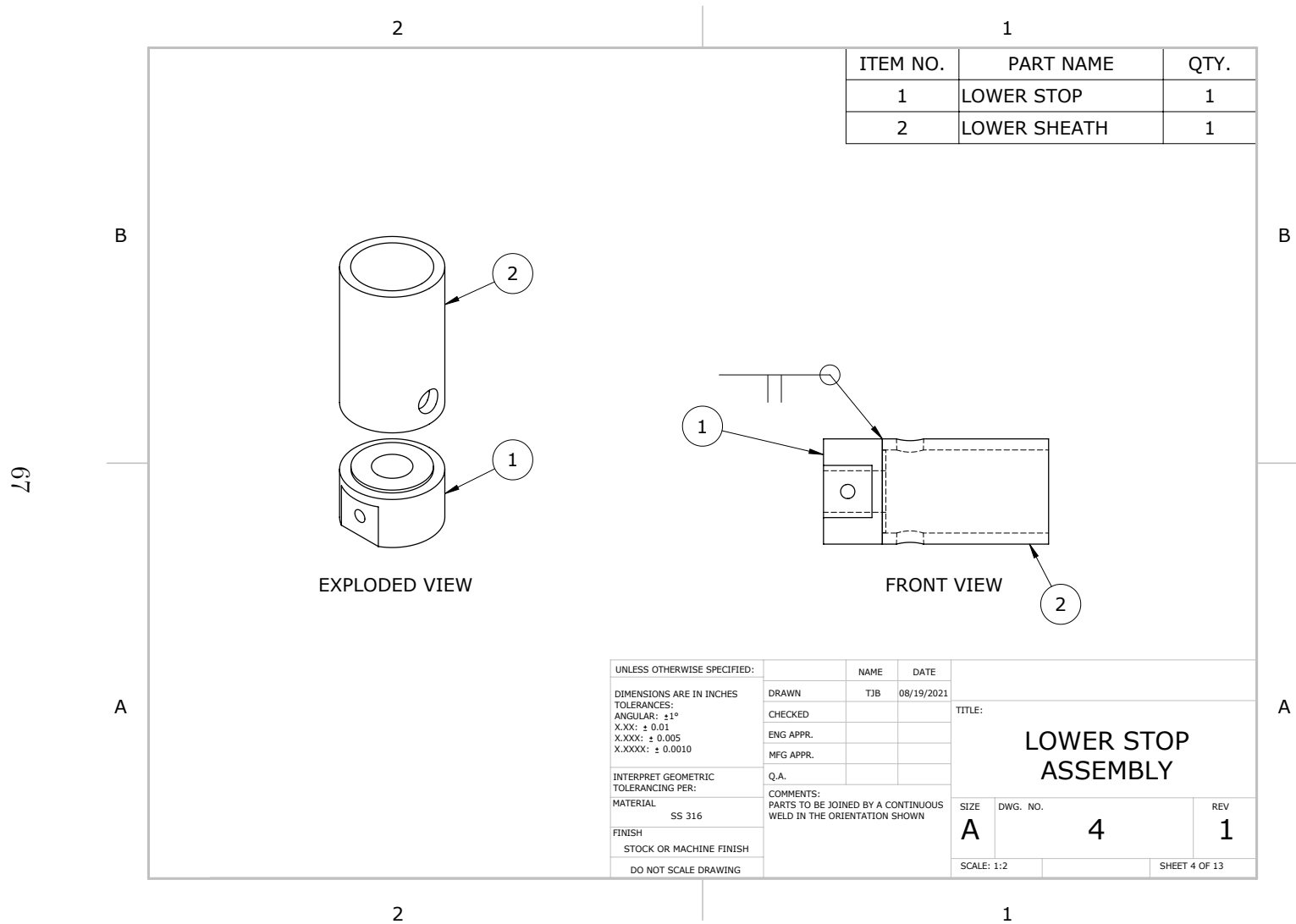


Figure A.4: Shown is the technical drawing for the lower stop assembly.

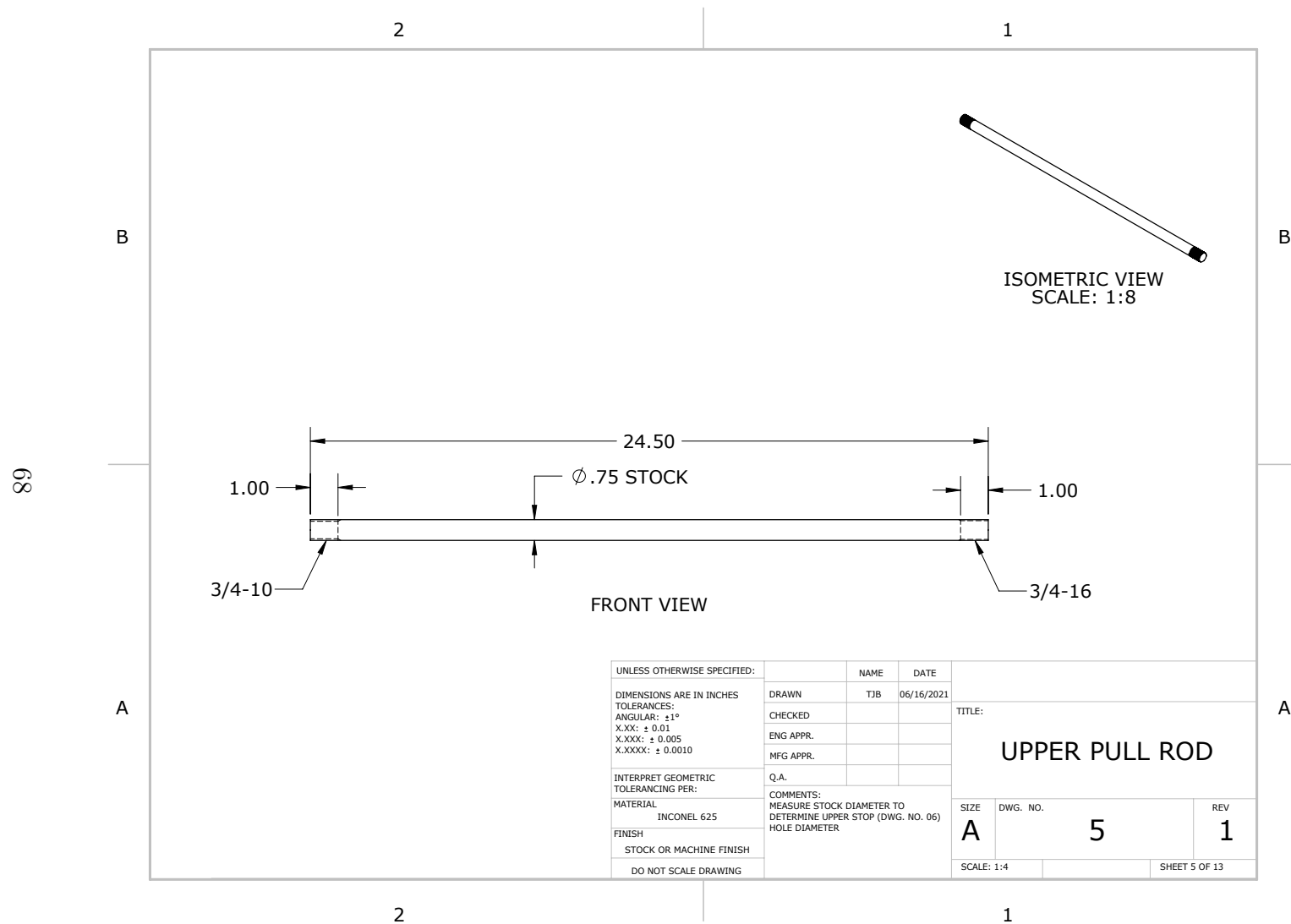


Figure A.5: Shown is the technical drawing for the upper pull-rod.

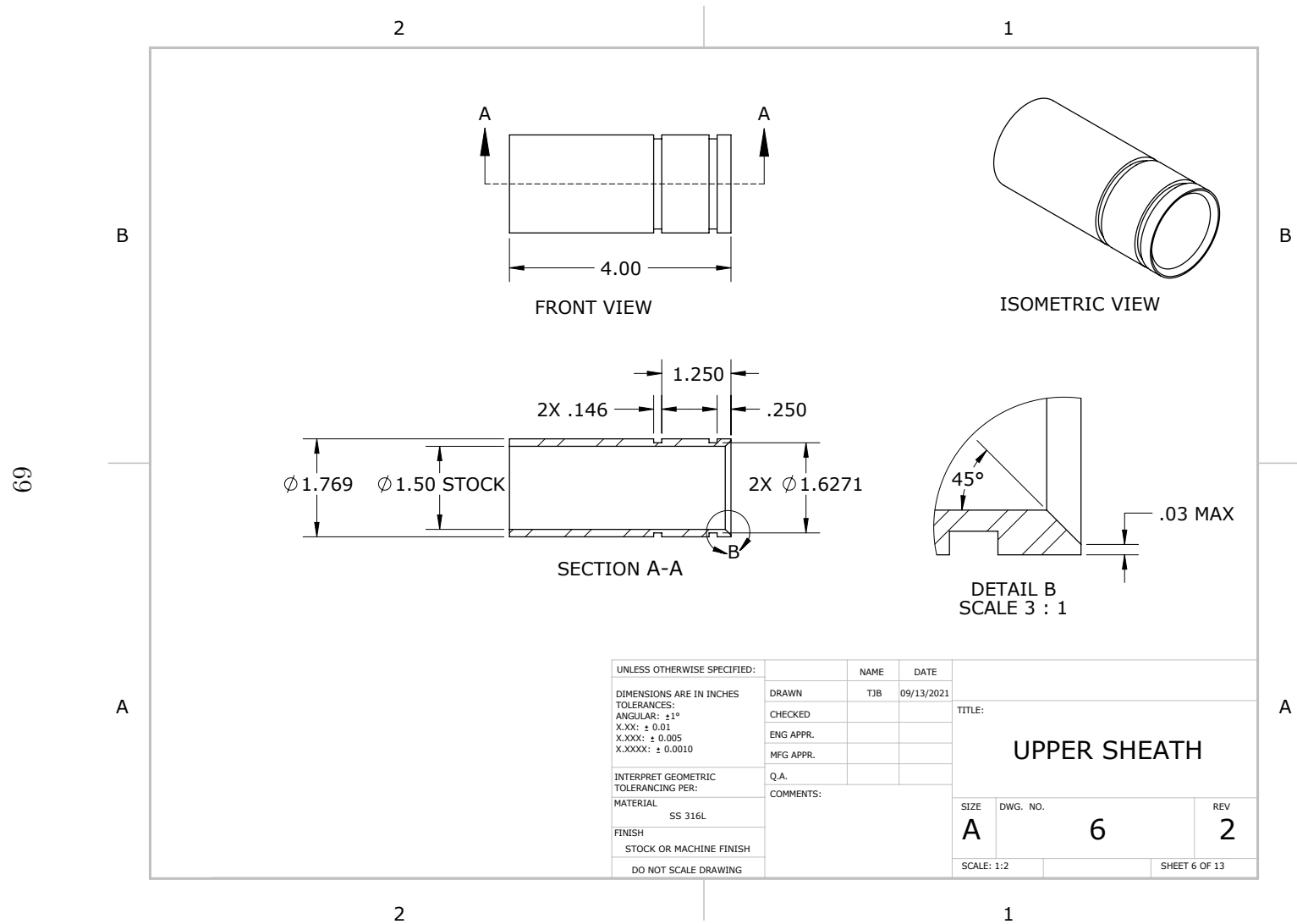


Figure A.6: Shown is the technical drawing for the upper sheath.

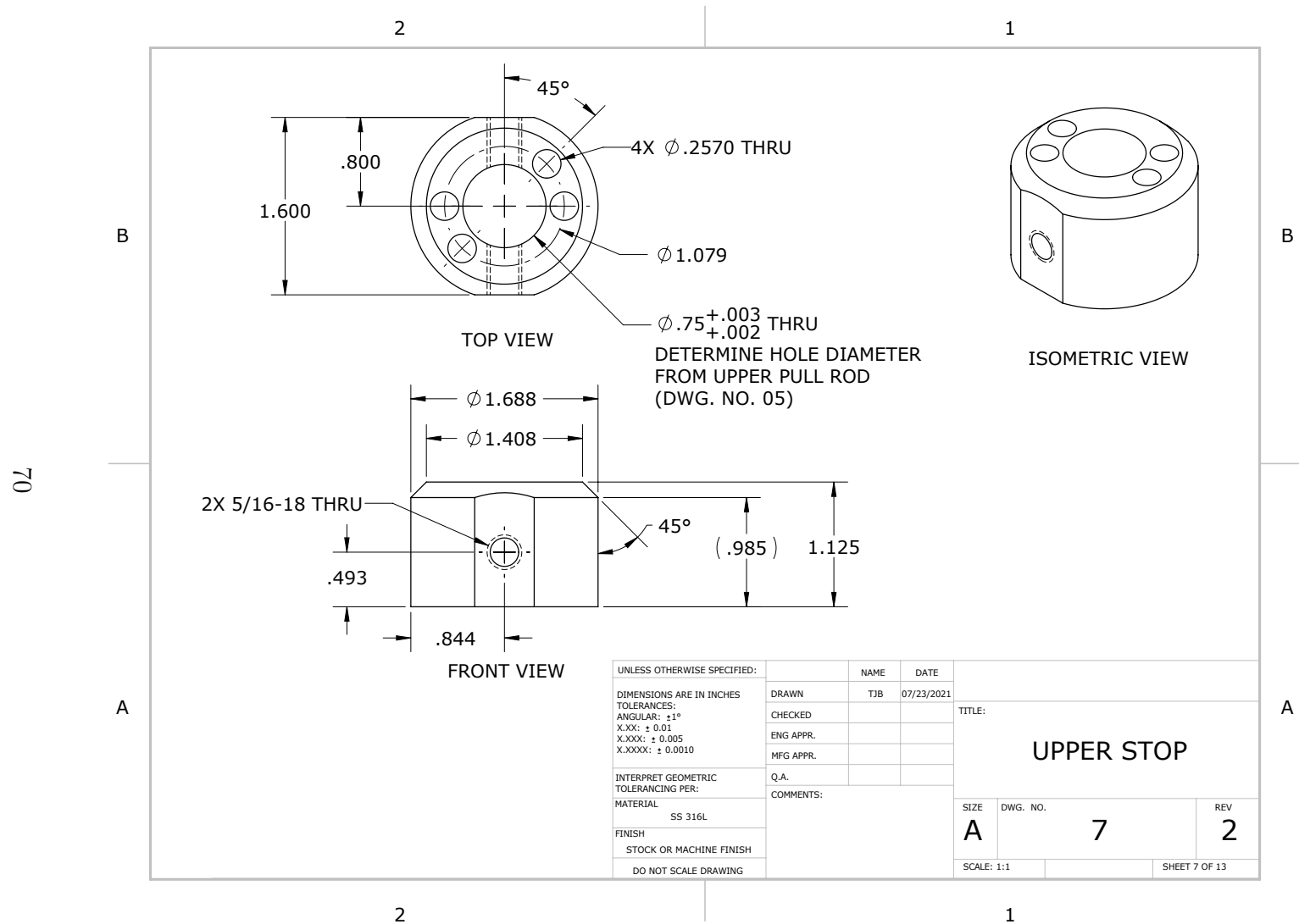


Figure A.7: Shown is the technical drawing for the upper stop.

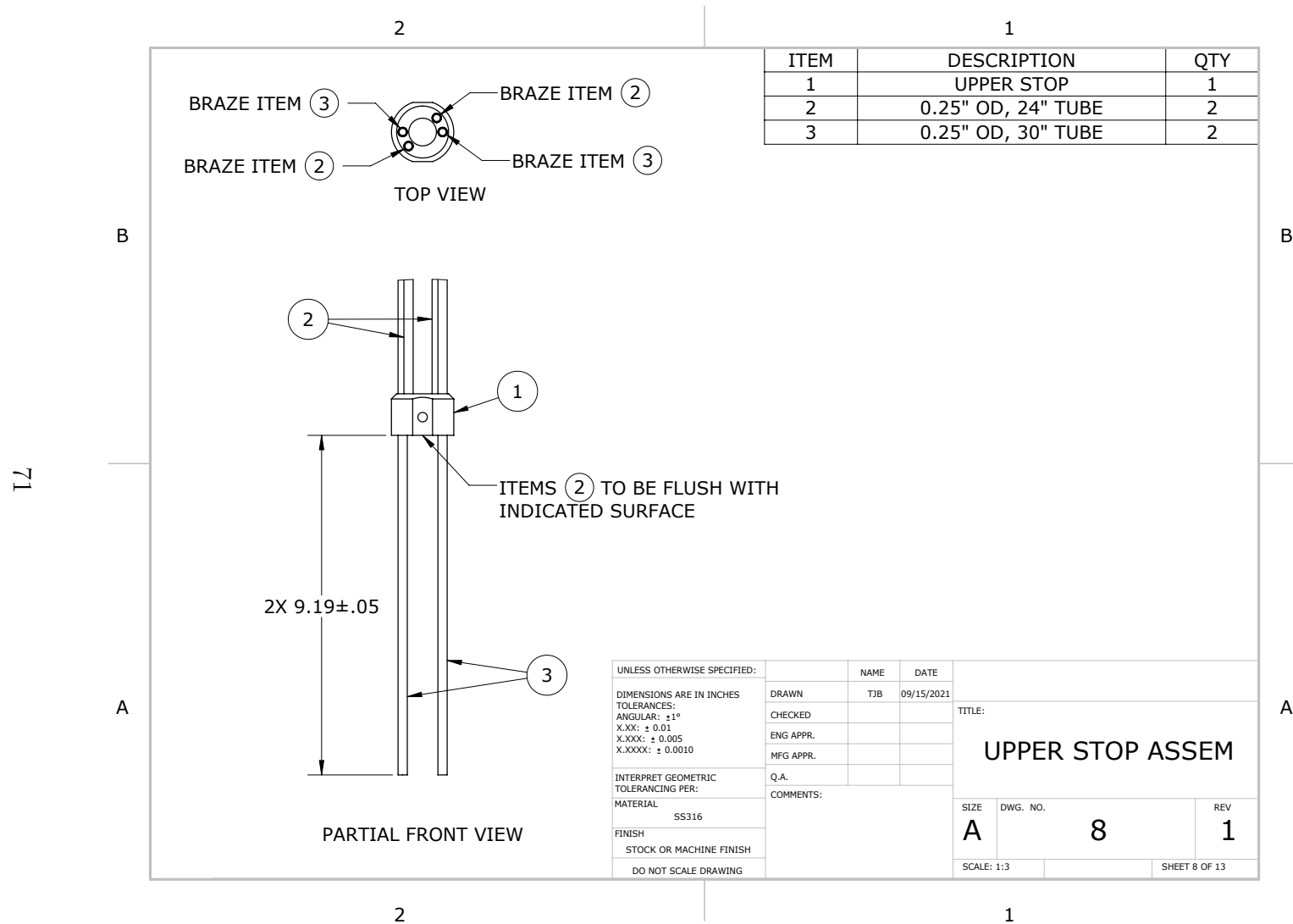


Figure A.8: Shown is the technical drawing for the upper stop assembly.

72

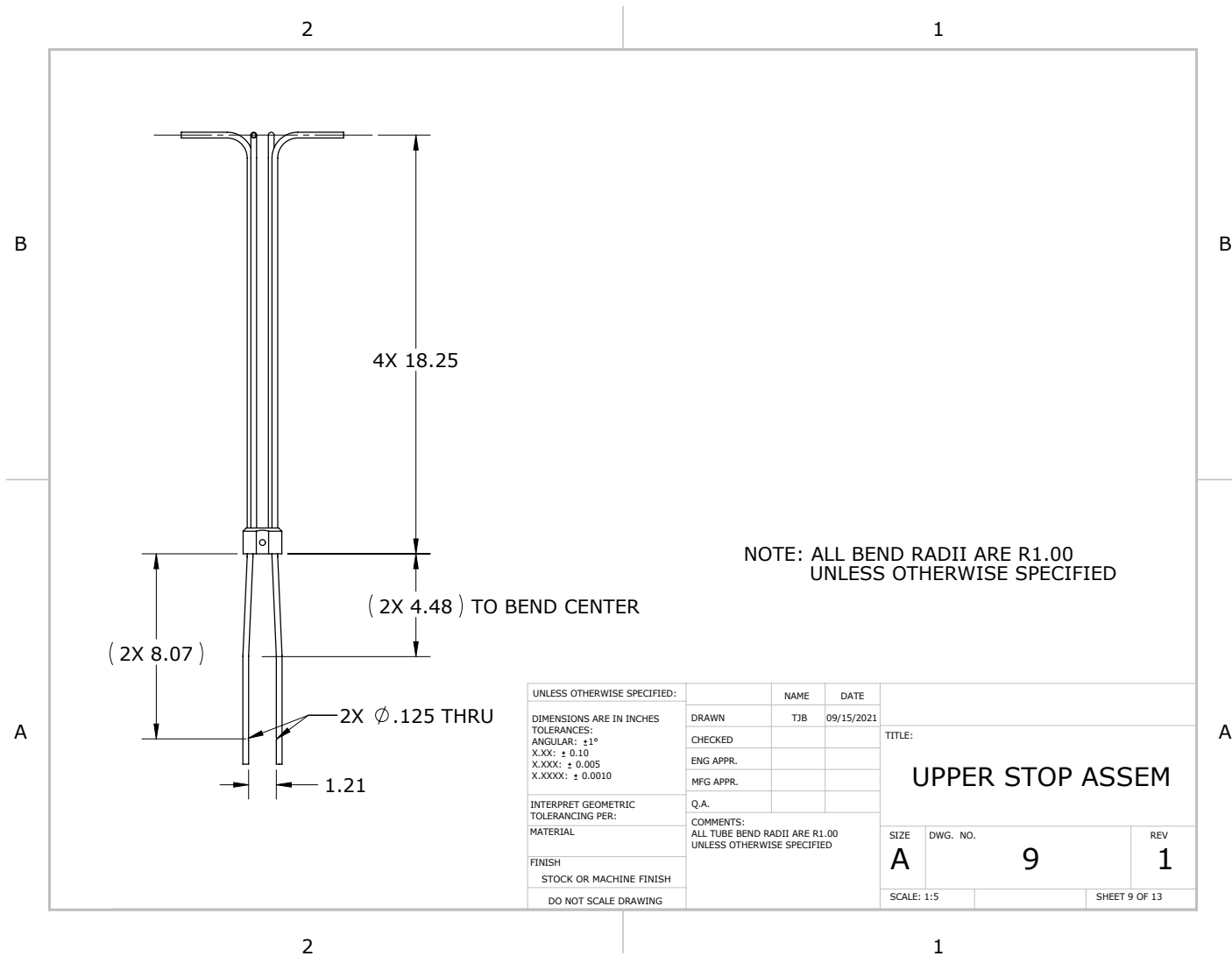


Figure A.9: This technical drawing shows the tube geometry for the upper stop assembly.

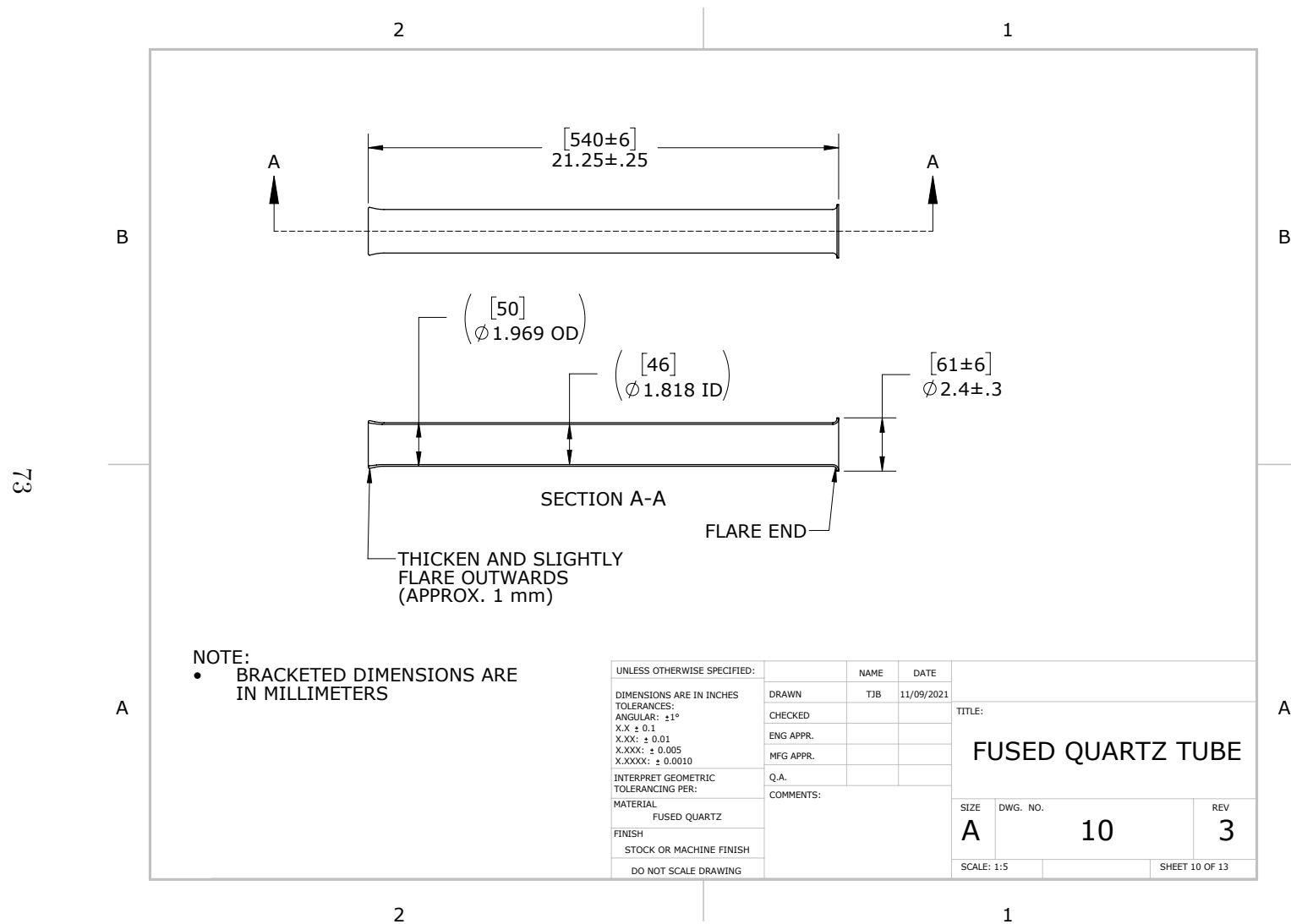


Figure A.10: Shown is the technical drawing for the quartz retort.

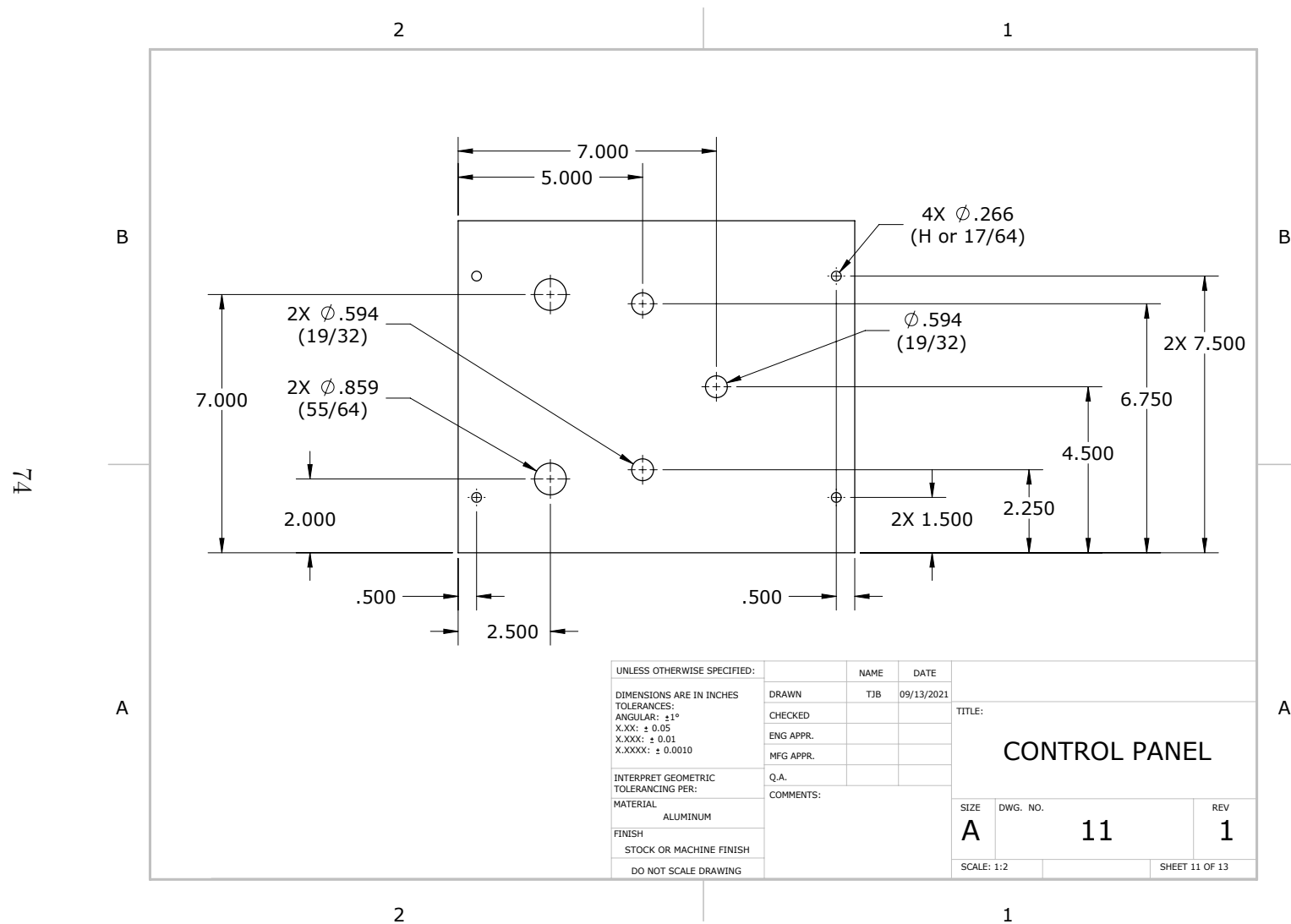


Figure A.11: Shown is the technical drawing for the flow control panel.

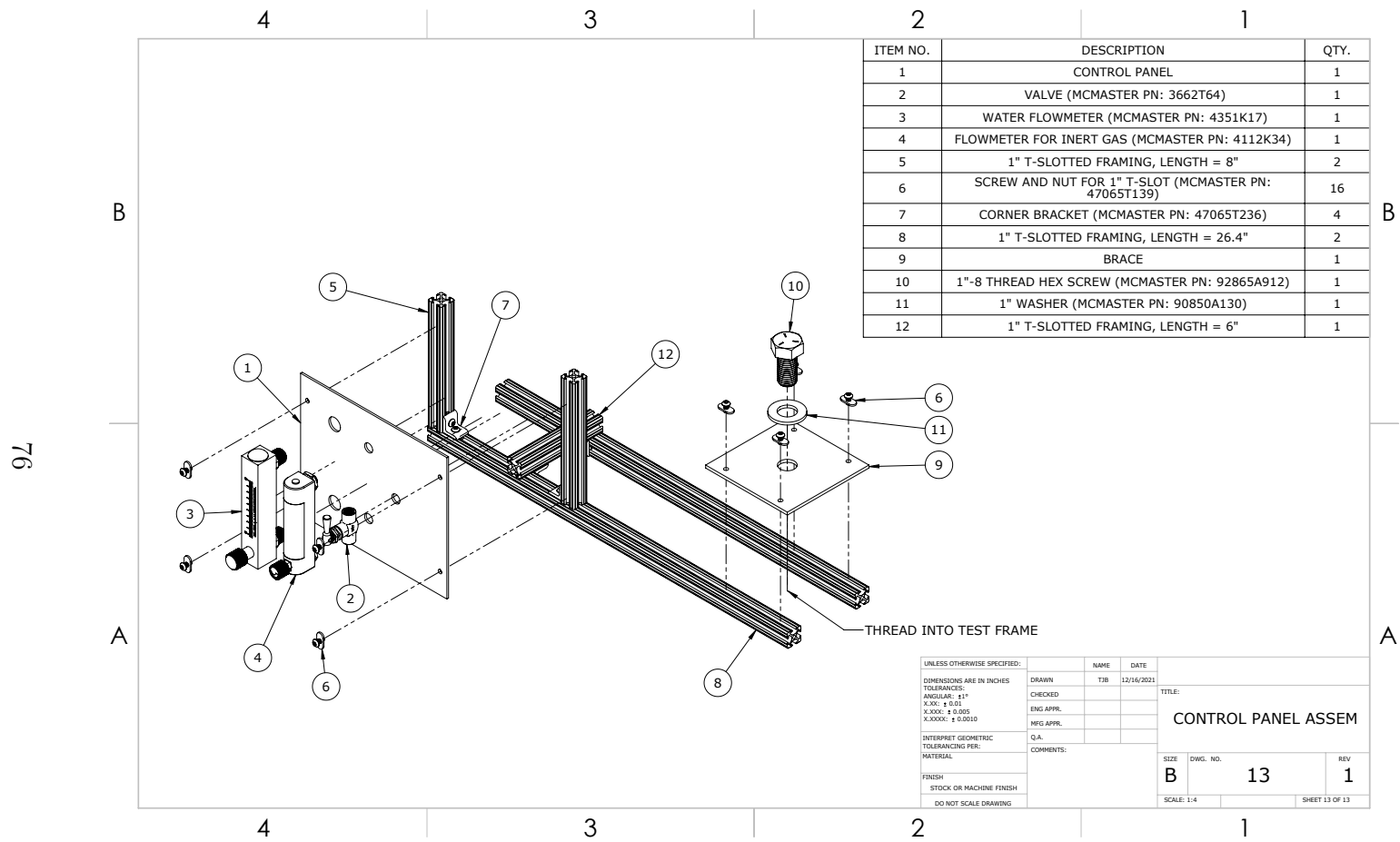


Figure A.13: Shown is the technical drawing for the flow control panel assembly.

Appendix B

Block Diagram and Python Script for Test Software Programming

B.1 Multipurpose Elite™ Block Diagram

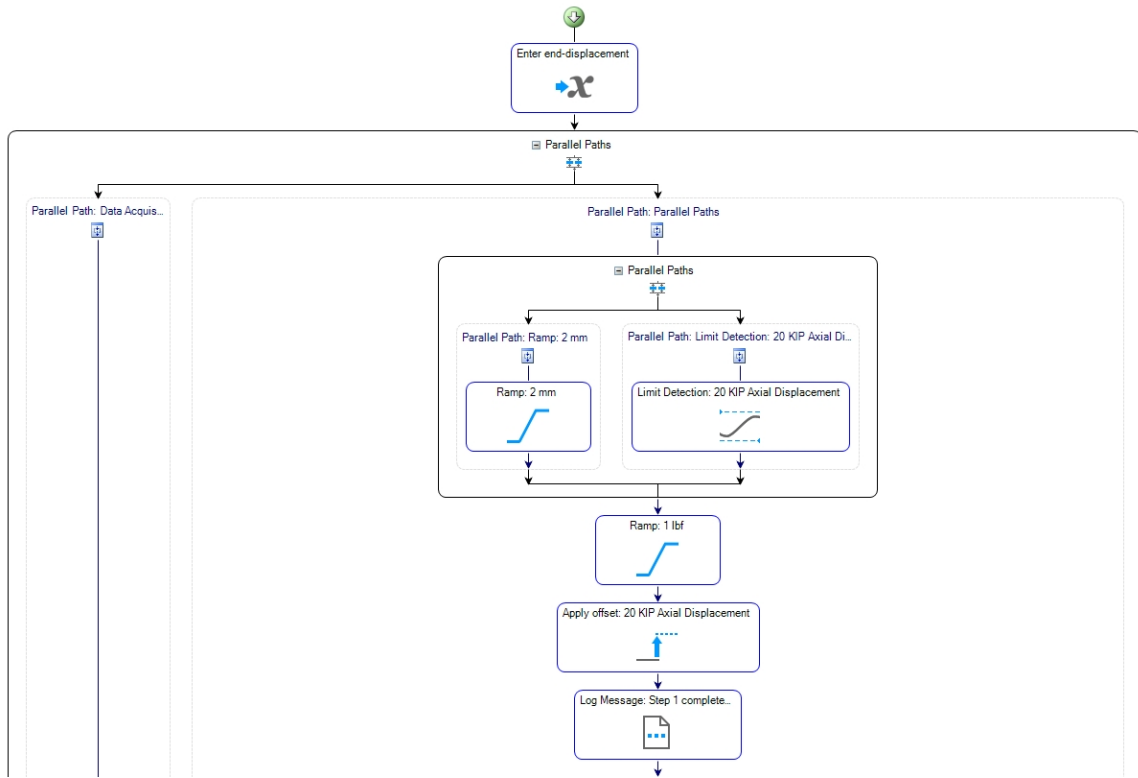


Figure B.1: Shown is the MTS Multipurpose Elite™ software block diagram for elevated-temperature tensile testing (Part 1).

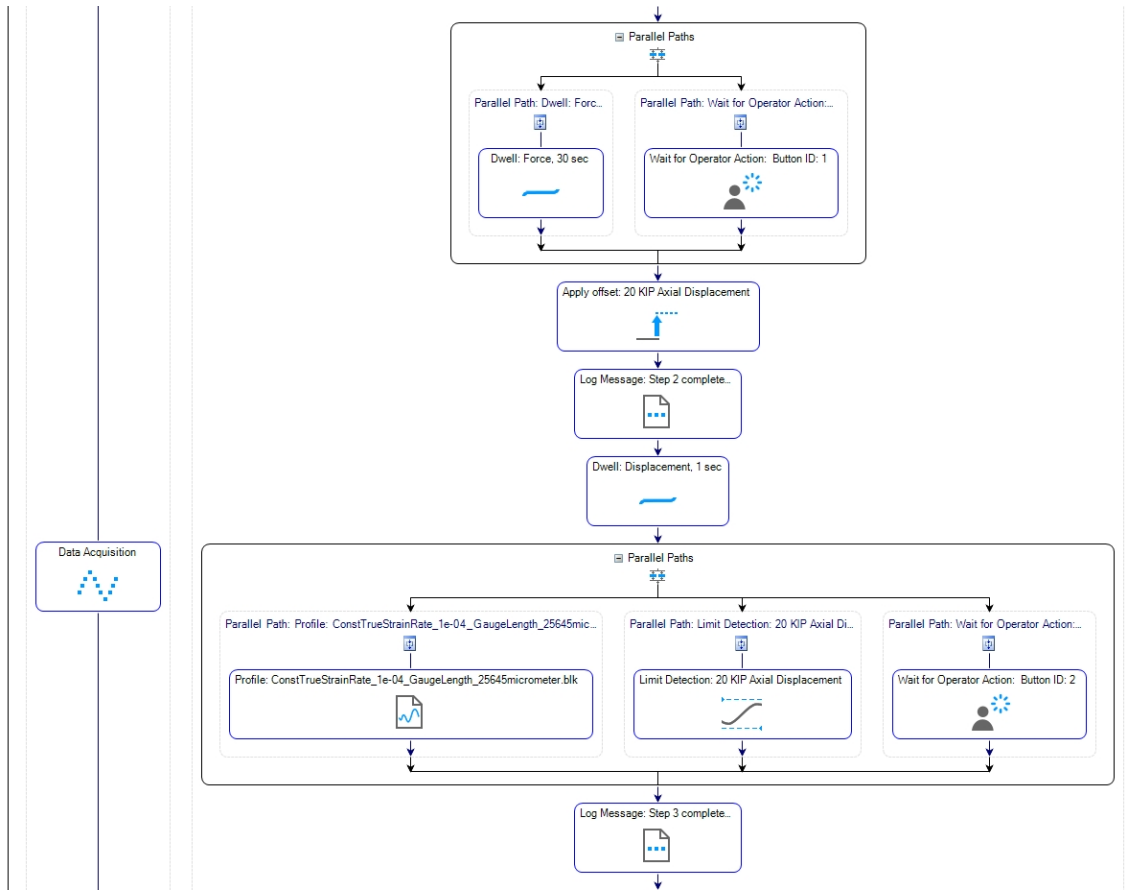


Figure B.2: Shown is the MTS Multipurpose Elite™ software block diagram for elevated-temperature tensile testing (Part 2).

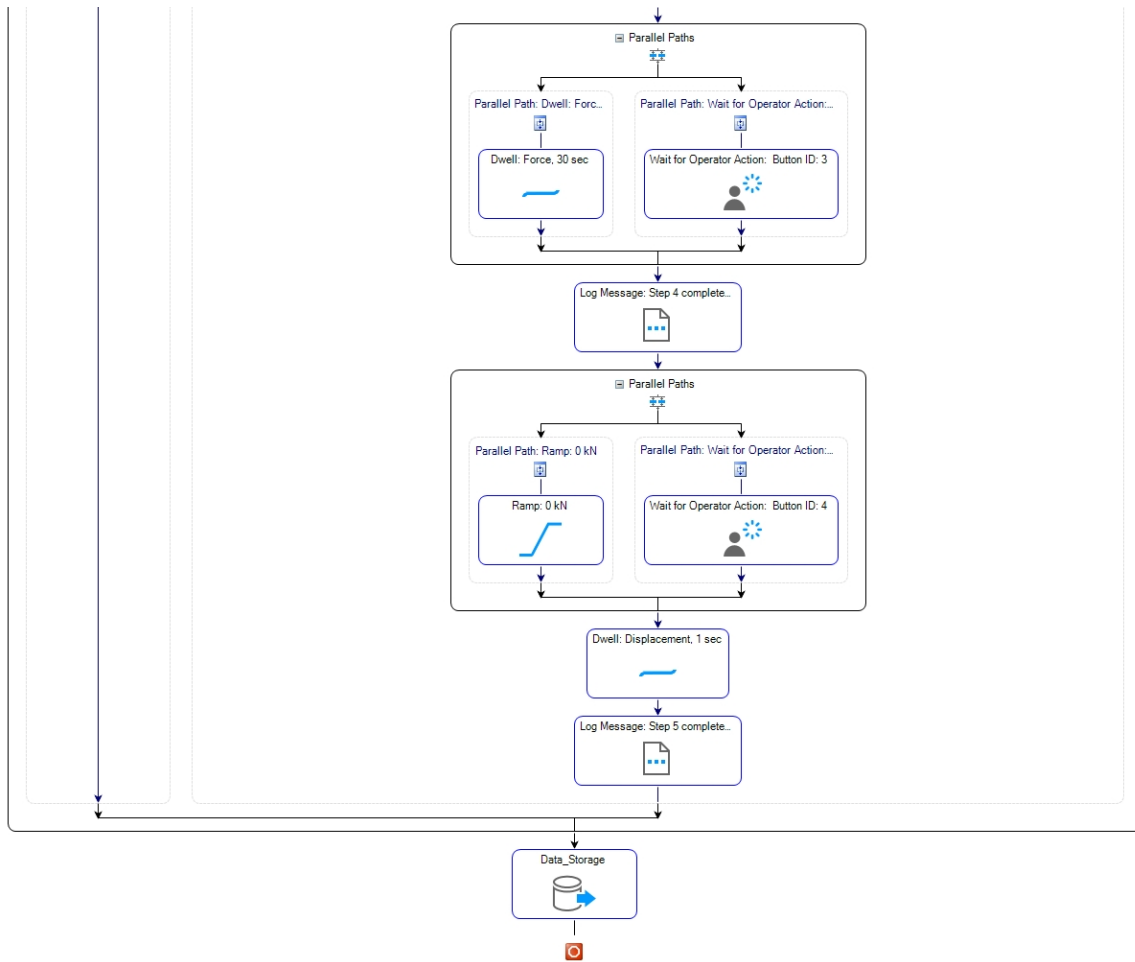


Figure B.3: Shown is the MTS Multipurpose EliteTM software block diagram for elevated-temperature tensile testing (Part 3).

B.2 Python Script for Generating a Displacement Profile

```
"""
```

```
This script generates a displacement profile  
in the form of a .blk file for the MTS MPE software  
given a desired true strain rate. The specimen gauge  
length, maximum displacement, and displacement  
increment are set by default. The user is  
prompted to manually overwrite these default values  
at runtime. The file 'header.txt' must be in the  
same directory as this script.
```

```
Written by Thomas Bennett, 2022-01-10
```

```
"""
```

```
import numpy as np
import datetime as dt

print("This program will generate a .blk file for the MTS MPE software  
given a desired true strain rate and certain geometric parameters (  
gauge length, total displacement, displacement profile increments).\n")

header = ''
i = 0
d = dt.date.today()
today = d.strftime("%Y_%m_%d")

# All lengths in mm
final_disp = 25.4
disp_step = 0.1
init_length = 25.4

print("Enter the desired true strain rate:")
tr_str_rate = float(input())

print("Default values:")
print("Gauge length = {:.1f} mm".format(init_length))
print("Displacement Increment = {:.1f} mm".format(disp_step))
print("Final Displacement = {:.1f} mm\n".format(init_length))
print("Use default values (No = 0, Yes = 1)?: ")
usedefaults = bool(int(input()))

if (not usedefaults):
    print("Enter the nominal specimen gauge length (mm): ")
```

```

init_length = float(input())

print("Enter the displacement increment (mm):")
disp_step = float(input())

print("Enter the final displacement (mm):")
final_disp = float(input())

with open('header.txt') as f:
    for lines in f:
        header = header + lines[:-1]
        if i == 1:
            header = header + today
        if i == 2:
            header = header + "True strain rate = {:.3e}; Specimen gauge
                length = {:.1f}".format(tr_str_rate, init_length)
            header = header + '\n'
            i = i + 1

disp = np.linspace(0, final_disp, int(np.round(final_disp / disp_step)) +
    1)
gauge_L = disp + init_length
disp_rate = (init_length + disp) * tr_str_rate

table_header = "\nRate\tLevel1\mmm/Sec\tmm\n"

table = ''
for i in range(len(disp)):
    if i == 0:
        table = table + "{:.7f}".format(disp_rate[i]) + '\t0\n'
    else:
        table = table + "{:.7f}".format(disp_rate[i]) + '\t' + \
            "{:.3f}".format(disp[i]) + '\n'
    # Last line has a newline character

filename = "ConstTrueStrainRate_{:.0e}_SpecLength_{:.0f}micrometer.blk".
    format(tr_str_rate, init_length*1000)

with open(filename, 'w') as f:
    f.write(header + table_header + table[:-1])

```

B.3 Displacement Profile Header File

A file named “header.txt” containing the following text must be placed in the same directory as the Python script provided in Appendix B.2.

```
FileType=Block-Arbitrary  
Date=  
Description=  
Channels=1
```

```
Channel(1)=20 KIP Axial  
Max=32.0000 mm  
Min=-10.0000 mm  
Shape=Ramp
```

Appendix C

Python Scripts for Mechanical Data Processing

```
"""
Data_extractor.py

This script loads raw mechanical data from the MTS MultiPurpose
Elite software. The data pertaining to heat-up, constant true-strain
rate deformation, and cool-down are saved in separate .txt files.
The raw data is imported from a .txt file beginning with 'raw.'

Written by Thomas Bennett
"""
import numpy as np
import matplotlib.pyplot as plt
import os
from UsefulFunctions_TB_20220126 import *

""" Input File Directory """

# Test data main directory
dir_main = "../Specimen_Data/"

for root, dirs_list, files in os.walk(dir_main):
    i = 1
    for dirs in dirs_list:
        print(str(i) + ': ' + str(dirs))
        i += 1
    break

print('\nEnter a number to select a folder')
i = int(input())
folder_test = dirs_list[i - 1]

# Test data directory
dir_test = dir_main + folder_test + '/'

# Find files to import
```

```

for root, dirs, files in os.walk(dir_test):
    for file in files:
        if file.startswith("raw"):
            file_test = root + '/' + file

# Check directories/paths
if not(os.path.isdir(dir_test)):
    raise RuntimeError('Invalid test file directory')
if not(os.path.isfile(file_test)):
    raise RuntimeError('Invalid bellows correction file directory')

# disp [mm], load [kN], time [sec]
[disp, load, time] = np.loadtxt(file_test, delimiter='\t', skiprows=8,
                               unpack=True)

# Parse the data for plotting
target_length = 5000
par_disp = data_parse(disp, target_length)
par_load = data_parse(load, target_length)
par_time = data_parse(time, target_length)

# Plot raw data values
fig, ax = plt.subplots(1,1)
ax.plot(par_time, par_disp, 'k')
ax.set(title = 'Extension vs. Time', xlabel = 'Time [s]',
        ylabel = 'Extension [mm]')
fig.tight_layout()
fig.show()

print('Enter the time [sec] before the tensile test starts')
start_time = float(input())

# Find breakpoints between heatup, testing, and cooldown
start_search = where(time, start_time, '>=')
test_start = start_search + where(disp[start_search:], 0.001, '<=')
ax.plot(time[test_start], disp[test_start], 'ro')
print("Test starts at index:", test_start)
test_end = test_start + where(disp[test_start:], max(disp[test_start:]),
                             '=')
print("Test ends at index:", test_end)
ax.plot(time[test_end], disp[test_end], 'ro')
fig.show()

fig, ax = plt.subplots(1,1)
ax.plot(par_disp, par_load, 'k')

```

```

ax.set(title = 'Load vs. Extension', ylabel = 'Load [kN]',
        xlabel = 'Extension [mm]')
fig.tight_layout()
fig.show()

# Save heatup, test, and cooldown data to separate files

file_out = dir_test + "heatup.txt"
header = 'Displacement\tLoad\tTime\mmm\tkN\tsec'
data_out = np.array((disp[:test_start], load[:test_start], time[:
    test_start])).T
np.savetxt(file_out, data_out, fmt='%%.12e', delimiter='\t', header =
    header)

file_out = dir_test + "test.txt"
data_out = np.array((disp[test_start:test_end],
    load[test_start:test_end],
    time[test_start:test_end])).T
np.savetxt(file_out, data_out, fmt='%%.12e', delimiter='\t', header =
    header)

file_out = dir_test + "cooldown.txt"
data_out = np.array((disp[test_end:], load[test_end:], time[test_end:])).T
np.savetxt(file_out, data_out, fmt='%%.12e', delimiter='\t', header =
    header)

print("Press [Enter] to exit")
input()

```

```
"""
```

```
Test_Analysis.py
```

```
This script processes the mechanical test data from elevated temperature tensile tests. Data must first be separated using "Data_extractor.py." The script loads the mechanical test data from a .txt file starting with 'test.' Specimen dimensions are input from 'spec_dims.txt,' which should be placed in the same directory as the test data.
```

```
The mechanical data is trimmed (this must be done manually by the user). A low-pass filter is applied to smooth the data. The total stiffness of the machine and specimen is determined by a linear fit (the user should verify that a good fit is achieved). Engineering and true stress-strain plots are generated. True strain is plotted against time.
```

```
Written by Thomas Bennett
```

```
"""
```

```
import numpy as np
import matplotlib.pyplot as plt
from matplotlib import ticker
import os
import sys
from UsefulFunctions_TB_20220126 import *

# Close plots
plt.close('all')

""" File Input """

# Test data main directory
dir_main = "../Specimen_Data/"

# Semi-automatic test data folder selection
for root, dirs_list, files in os.walk(dir_main):
    i = 1
    for dirs in dirs_list:
        print(str(i) + ': ' + str(dirs))
        i += 1
    break

print('\nEnter a number to select a folder')
i = int(input())
folder_test = dirs_list[i - 1]
```

```

# Test data directory
dir_test = dir_main + folder_test + '/'

# Find files to import
for root, dirs, files in os.walk(dir_test):
    for file in files:
        if file.startswith("test"):
            file_test = root + '/' + file
        if file.startswith("spec_dims"):
            file_params = root + '/' + file

# Check directories/paths
if not(os.path.isdir(dir_test)):
    raise RuntimeError('Invalid_test_file_directory')
if not(os.path.isfile(file_test)):
    raise RuntimeError('Invalid_test_data_file_path')
if not(os.path.isfile(file_params)):
    raise RuntimeError('Invalid_specimen_parameter_file_path')

# For printing console output to a text file
f = open(dir_test + 'print_output2.txt', 'w')

# Original Units disp [mm], load [kN], time [sec]
[disp, load, time] = np.loadtxt(file_test, delimiter='\t', skiprows=8,
                                unpack=True)

n = len(disp) # Length of the dataset
time = time - time[0] # Zero the start time

### Unit conversions ###
# Convert load to kN
load = load * 1000

# Import specimen dimensions from parameters file
params = np.loadtxt(file_params, delimiter='_=_', dtype=str,
                    usecols=(0,1))

print(folder_test, file=f)

""" Plotting Parameters """

figw = 5.2
figh = 3.25

# Plotting parameters

```

```

plt.rcParams.update({
    "figure.figsize": [figw,figh],
    "text.usetex": True,
    "font.family": "serif",
    "axes.grid": False,
    "axes.grid.which": "major",
    "axes.titlesize": 12,
    "axes.labelsize": 12,
    "figure.subplot.hspace": 0.35,
    "xtick.minor.visible": True,
    "ytick.minor.visible": True})

""" Analysis """

# Specimen Geometry Calculations
glen = float(params[1,1]) * 25.4 # [mm]
gwid = float(params[2,1]) * 25.4 # [mm]
gthick = float(params[3,1]) * 25.4 # [mm]
gArea = gwid * gthick

# Specimen Geometry at temperature
temp = float(params[4,1]) + 273.15 # Kelvin
room_temp = 22 + 273.15
coef_therm_exp = 0.0000117 # 1/Kelvin
glenT = glen * (1 + coef_therm_exp * (temp - room_temp))
gwidT = gwid * (1 + coef_therm_exp * (temp - room_temp))
gthickT = gthick * (1 + coef_therm_exp * (temp - room_temp))
gAreaT = gwidT * gthickT

# Plot the data so it may be trimmed
fig1, ax1 = plt.subplots(1,1)
ax1.plot(displacement, load, 'k')
ax1.set(title = 'Load vs. Extension', ylabel = 'Load [N]',
        xlabel = 'Extension [mm]')
fig1.tight_layout()

fig2, ax2 = plt.subplots(1,1)
ax2.plot(time, load, 'k')
ax2.set(title = 'Load vs. Time', xlabel = 'Time [s]',
        ylabel = 'Load [N]')
fig2.tight_layout()

# Trim the data; a = start, b = stop
a = 0 # default 0
b = n # default n

```

```

## Uncomment below and enter start and end times [sec] to trim data
# start_t = 1.2
# end_t = 950
# a = where(time, start_t, '>=')
# b = where(time, end_t, '>=')
# print('\nStart/End = {:.f}/ {:.f} seconds '.format(start_t, end_t), file=f)
disp = disp[a:b]
load = load[a:b]
time = time[a:b]
time = time - time[0]
n2 = len(disp) # Get the new number of data points

#Elastic Modulus Calculation
E_mod = 9.80665 * (33400.54 - temp * 19.18677) # MPa from Koster
print('\nElastic Modulus [GPa]: {:.3f}'.format(E_mod / 1000))
print('\nElastic Modulus [GPa]: {:.3f}'.format(E_mod / 1000), file=f)
spec_stiffness = E_mod * gAreaT / glenT # N/mm
a = where(disp, 0.0, '>=') # start of elastic region
b = where(disp, 0.008, '>=') # end of elastic region
total_stiffness, load_intercept = LinearReg(disp[a:b], load[a:b])[0:2]
print('Total Stiffness [N/mm]: {:.3f}'.format(total_stiffness))
print('Total Stiffness [N/mm]: {:.3f}'.format(total_stiffness), file=f)

# Plot the fit curve for the elastic region
ax1.plot(disp[a:b], total_stiffness * disp[a:b] + load_intercept, 'r-')

# Correct starting displacement
disp = disp + load_intercept / total_stiffness
print('Displacement Correction [mm]: {:.3f}'.format(load_intercept /
total_stiffness))
print('Displacement Correction [mm]: {:.3f}'.format(load_intercept /
total_stiffness), file=f)
machine_stiffness = 1 / (1 / total_stiffness - 1 / spec_stiffness)
print('Machine Stiffness [N/mm]: {:.3f}'.format(machine_stiffness))
print('Machine Stiffness [N/mm]: {:.3f}'.format(machine_stiffness),
file=f)

# Filter the data
m = 50
c = 150
freq = m / (time[m] - time[0])
cutoff = .25
disp_f = np.zeros(n2)
load_f = np.zeros(n2)

```

```

load_f[:] = load[:]
disp_f = low_pass_window(disp, freq, cutoff, binsize=2**12, overlap=0.25,
    order=2)
load_f[c:] = low_pass_window(load[c:], freq, cutoff, binsize=2**12,
    overlap=0.25, order=2)

# Parse the data again
target_length = 1000
disp_par = data_parse(disp, target_length)
target_length = len(disp_par) # redefine the target length because the
    data cannot be evenly parsed
load_par = data_parse(load, target_length)
disp_par_f = data_parse(disp_f, target_length)
load_par_f = data_parse(load_f, target_length)
time_par = data_parse(time, target_length)

## Uncomment to plot unfiltered and filtered data
# fig3, ax3 = plt.subplots(1,1)
# ax3.plot(time_par/60, disp_par, 'k')
# ax3.plot(time_par/60, disp_par_f, 'r')
# ax3.set(title = 'Displacement vs. Time', xlabel = 'Time [min]',
#         ylabel = 'Displacement [mm]')
# fig3.tight_layout()
# fig4, ax4 = plt.subplots(1,1)
# ax4.plot(time_par/60, load_par, 'k')
# ax4.plot(time_par/60, load_par_f, 'r')
# ax4.set(title = 'Load vs. Time', xlabel = 'Time [min]',
#         ylabel = 'Load [N]')
# fig4.tight_layout()

# Plot load vs. extension
fig5, ax5 = plt.subplots(1,1)
ax5.plot(disp_par, load_par_f, 'k')
ax5.set(title = 'Load vs. Extension', xlabel = 'Extension [mm]',
        ylabel = 'Load [N]')
fig5.tight_layout()
# fig5.savefig("Load_Extension.svg")

""" Stress and Strain Calculations """

# Force the load and displacement to start at the origin
disp_par_f[0] = 0
load_par_f[0] = 0

# Calculate stress and strain

```

```

Estrain = disp_par_f / glenT
Tstrain = np.log(1 + Estrain)
Estress = load_par_f / gAreaT #[MPa]
Tstress = Estress * (1 + Estrain)

""" True Strain Rate Calculation and Plot """

# Caculate true strain with raw data
Tstr2 = np.log(1 + disp / glenT)

# Calculate the true-strain rate with linear regression
TstrainRate, Tstr_intercept, rsqrd = LinearReg(time, Tstr2)

print("The true strain rate is: {:.4e}s-1".format(TstrainRate))
print("The true strain rate is: {:.4e}s-1".format(TstrainRate), file=f)
print("The true strain rate r-squared is: {:.14f}".format(rsqrd))
print("The true strain rate r-squared is: {:.14f}".format(rsqrd), file=f)

# Plot the true strain against time
fig6, ax6 = plt.subplots(1,1)
ax6.plot(time, Tstr2, 'k', linewidth = 4)
ax6.plot(time, TstrainRate * time + Tstr_intercept, 'r--')
ax6.set(xlabel = 'Time [s]',
        ylabel = 'True Strain [-]')
max_time = np.ceil(max(time)/100) * 100
ax6.set_xlim(0)
ax6.set_ylim(0)
ax6.spines["right"].set_visible(False)
ax6.spines["top"].set_visible(False)
ax6.legend(["Measured True Strain", "Linear Fit"], fontsize = 11)
equation = "$\varepsilon = \left( {:.4f} \right) \cdot \text{format}(TstrainRate*1E4)$"
equation = equation + "\times 10^{-4} \right) t$"
ax6.text(800,.03,equation, fontsize = 11)
fig6.tight_layout()
fig6.savefig(dir_test + params[0,1] + '_tstrain_time.pdf')

""" Stress-Strain Plots """

# Plot engineering stress vs. strain
fig7, ax7 = plt.subplots(1,1)
ax7.plot(Estrain, Estress, 'k')
ax7.set(title = 'Engineering Stress vs Strain', xlabel = 'Engineering Strain [-]',
        ylabel = 'Engineering Stress [MPa]')
fig7.tight_layout()

```

```

# Plot true stress vs. strain
fig8, ax8 = plt.subplots(1,1)
ax8.plot(Tstrain, Tstress, 'k')
ax8.grid(True)
ax8.set(xlabel = 'True Strain[-]',
        ylabel = 'True Stress[MPa]')
ax8.spines["right"].set_visible(False)
ax8.spines["top"].set_visible(False)
ax8.set_xlim(0)
ax8.set_ylim(0)
fig8.tight_layout()
fig8.savefig(dir_test + params[0,1] + '_tstress_tstrain.pdf')

# Average flow stress calculation
a = where(Tstrain, .05, '>=')
avg_flow = np.mean(Tstress[a:])
print('The average flow stress is {:.3f} MPa.'.format(avg_flow))
print('The average flow stress is {:.3f} MPa.'.format(avg_flow), file=f)
print('The final true strain is {:.5f}'.format(Tstrain[-1]))
print('The final true strain is {:.5f}'.format(Tstrain[-1]), file=f)

f.close() # Close the print output file

```

```

"""
Companion functions

Written by Thomas Bennett, 2021-09-24

* Some functions based on "UsefulFunctions20180703.R" by Eric Taleff

Updated: 2021-11-05
    - Correction in butterworth_lowpass

Updated: 2022-01-05
    - Added 'data_parse()' function
    - Changed default method to '>=' in 'where()' function

Updated: 2022-01-26
    - Added 'moving_average()' function
"""

import numpy as np

"""
where(x, a, method = '='):

    Function returns the index 'i' at which the value x[i] in the array
    'x' is equal to the value of 'a'. By changing the method to either
    '<' or '>', the smallest index 'i' for which the x[i] is
    less/greater (respectively) than 'a' is returned. The methods '<='
    and '>=' are also supported.

    Written by Thomas Bennett, 2021-09-25
"""

def where(x, a, method = '>='):
    n = len(x)

    # '=' method
    if method == '=':
        for i in range(n):
            if x[i] == a: return i
        raise RuntimeError("No value of 'x' that is equal to " + str(a))

    # '<' method
    elif method == '<':
        for i in range(n):
            if x[i] < a: return i

```

```

        raise RuntimeError("No value of 'x' that is less than" + str(a)
            )

# '>' method
elif method == '>':
    for i in range(n):
        if x[i] > a: return i
    raise RuntimeError("No value of 'x' that is greater than" + str
        (a))

# '<=' method
elif method == '<=':
    for i in range(n):
        if x[i] <= a: return i
    raise RuntimeError("No value of 'x' that is less than/equal to"
        + str(a))

# '>=' method
elif method == '>=':
    for i in range(n):
        if x[i] >= a: return i
    raise RuntimeError("No value of 'x' that is greater than/equal
        to"
            + str(a))

else:
    raise RuntimeError("method does not support value"
        + str(method) + "'")

"""
LinearReg(x, y):

    Function that performs least-squares linear regression on the arrays
    'x' and 'y' using the model 'y = ax + b'. The values of 'a' and 'b'
    are returned as 'slope' and 'intercept' respectively along with the
    square of the correlation coefficient ( $R^2$ ) as 'rsqr'.

    Written by Thomas Bennett, 2021-09-24
"""

def LinearReg(x, y):

    # Check that x and y are the same length
    if len(x) != len(y): raise RuntimeError("'x' and 'y' must have the"
        +

```

```

"same_length")

# Construct matrices for the least-squares linear regression problem
A = np.array ([[sum(x ** 2), sum(x)],
               [sum(x), len(x)]])
B = np.array ([[sum(x * y)],
               [sum(y)]])

# Solve the LSLR problem
[slope, intercept] = np.linalg.solve(A,B)

# Model y to calculate the correlation coefficient
y_model = slope * x + intercept

# Calculate the correlation coefficient and rsqrd
corrcoef = (np.average(y * y_model) - np.average(y) *
            np.average(y_model)) / np.std(y) / np.std(y_model)
rsqrd = corrcoef ** 2

return slope[0], intercept[0], rsqrd

"""
FindPeaks(x, m = 3):

Function that determines the locations of peak values (local maxima)
in an array 'x'. A value is determined to be a peak value if it is
the maximum value in a window of size 2m + 1 centered on that value.
An array named 'peaks' containing the indices for which 'x' has a
peak value is returned. The length of 'peaks' is equal to the number
of peaks in 'x'.

Based on 'findpeaks' by Eric Taleff

Converted and edited by Thomas Bennett, 2021-09-24
"""

def FindPeaks(x, m = 3):

# Initialize 'peaks' array
peaks = []

# Loop through x to find peaks
for i in range(len(x)):

# Set lower and upper indices

```

```

    low = int(i - m)
    up = int(i + m + 1)

    # Correct indices at array start/end
    if low < 0: low = 0
    if up > len(x): up = len(x)

    if x[i] == max(x[low:up]):
        peaks.append(i)

return peaks

"""
lslrDeriv(x, y, m = 3):

    Function that calculates the derivative at a point x[i] in an array
    'y' of length equal to that of 'x'. The derivative/slope is
    calculated by computing the least-squares linear regression slope
    using the points in a window of size 'm' (odd) centered on x[i].
    Two arrays with lengths less than that of 'x' and 'y' are returned
    containing values of 'x' and the slope values from 'y'. These
    arrays are denoted 'x_new' and 'slopes' respectively.

    Based on 'slopescalc' by Eric Taleff

    Converted and edited by Thomas Bennett, 2021-09-25
"""

def lslrDeriv(x, y, m = 3):

    # Check that x and y are the same length
    if len(x) != len(y): raise RuntimeError(" 'x' and 'y' must have the
        +
                                                "same length")

    # Make m odd if it is not already
    if m % 2 == 0: m += 1

    # Setup variables for indexing
    n = len(x)
    half_m = int(m/2)

    # Create shortened arrays for the x values and slopes
    x_new = np.zeros(n - 2 * half_m)
    slopes = x_new.copy()

```

```

    # Loop through the arrays and calculate the slopes using LinearReg
    for i in range(n - 2 * half_m):
        x_new[i] = x[i + half_m]
        slopes[i] = LinearReg(x[i:(i+m)], y[i:(i+m)])[0]

    return x_new, slopes

"""
def data_parse(x, target_length):

    Function that reduces the length of an array 'x' to the target
    length by discarding intermediate values. Kept values are
    equispaced. The returned array is denoted 'y'.

    Written by Thomas Bennett, 2021-09-28
"""

def data_parse(x, target_length):

    # Get the length of the input array ('n')
    n = len(x)

    # Calculate the reducing factor 'k' that will get the new array
    # closest to
    # the target length.
    k = int(round(n / target_length))

    # Check k
    if k <= 0: k = 1

    # Calculate the length of the new array 'y' ('m')
    m = int((n - 1) / k) + 1

    # Initialize 'y'
    y = np.zeros(m)

    # Parse the data
    for i in range(m):
        y[i] = x[i*k]

    return y

"""
butterworth_lowpass(signal, freq, cutoff, order = 2):

```

Called by low_pass_window. Not intended to be directly called.

Function that applies a Butterworth low-pass filter of specified order to an array 'signal' of data points collected at a constant sampling frequency. Inputs are the 'signal' to be filtered, the sampling frequency 'freq', the low-pass cutoff frequency 'cutoff' (same units as 'freq'), and the 'order' of the Butterworth filter. Note that 'order' must be a positive integer. Increasing the order makes the filter more aggressive, but can lead to more artifacts in the data. Use a high-order filter on consistent high-frequency noise and a low-order filter on more random noise.

Written by Thomas Bennett, 2021-09-26

Update 1: 2021-11-05

Corrected frequency domain vector 'xf'

"""

```
def butterworth_lowpass(signal, freq, cutoff, order = 2):

    n = len(signal)
    ct = int(np.ceil(cutoff/freq*n))
    sigf = np.fft.fft(signal) # Fourier transform of the signal

    xf = np.linspace(0, n-1, n) * 1j / ct # Frequency domain vector

    # Initialize the normalized Butterworth polynomial
    B = 1

    # Create the normalized Butterworth polynomials
    for i in range(int(order/2)):
        B = B * (xf ** 2 - 2 * xf * np.cos(np.pi * (2 * i + order + 1) /
                                           (2 * order)) + 1)

    if order % 2 == 1:
        B = B * (xf + 1)

    H = 1/B # Filter function in the frequency domain

    index = int(np.floor(n / 2)) + 1 # Index at midpoint of DFT freq
    domain

    # Apply the lowpass filter in the frequency domain
    for i in range(index):
        sigf[i] = abs(H[i]) * sigf[i]
```

```

# Force the proper symmetry of the Discrete Fourier Transform
for i in range(index-1):
    sigf[n-1-i] = sigf[i+1].real - 1j * sigf[i+1].imag

# Take the inverse FFT and return it
new_sig = np.fft.ifft(sigf).real

return new_sig

"""
low_pass_window(signal, freq, cutoff, binsize=2**11, overlap=0.2, order
= 2):

    Function that applies a Butterworth low-pass filter of specified
    order to an array 'signal' of data points collected at a constant
    sampling frequency. The input 'signal' is filtered in overlapping
    sections to increase efficiency and reduce artifacts from the
    IFFT. Inputs are the 'signal' to be filtered, the sampling
    frequency 'freq', the low-pass cutoff frequency 'cutoff' (same
    units as 'freq'), the 'binsize' (length) of each section, the
    'overlap' between sections, and the 'order' of the Butterworth
    filter. If artifacts appear in the filtered data (due to a very
    low cutoff frequency), increase the 'overlap'.

    Written by Thomas Bennett, 2021-09-26

"""

def low_pass_window(signal, freq, cutoff, binsize=2**11, overlap=0.2,
order = 2):

    # Get the length of the signal
    n_sig = len(signal)

    # Correct overlap if larger than one
    if overlap > 1:
        overlap = 1

    # Reduce the binsize if it is too large
    if binsize > (len(signal) + binsize * overlap):
        if overlap < 1:
            # Reduced bin size
            binsize = int(np.floor((len(signal)) / (1 - 1 * overlap)))

    n_bin = int(np.ceil(n_sig / (binsize * (1 - overlap)))) # Number of

```

```

        bins
n_overlap = int(np.floor(binsize * overlap)) # Number of overlap
        points

# Add buffers before and after the signal
signal = np.concatenate((np.ones(n_overlap) * np.mean(signal[0]),
        signal, np.ones(n_overlap) * np.mean(signal[-1])))

# Initialize the filtered signal array
sig_filt = np.zeros(n_sig)

# Define indices for array slicing
j1 = 0
j2 = j1 + binsize
j3 = j2 - n_overlap

s1 = int(n_overlap / 2)
s2 = s1 + j3 - j1

for i in range(n_bin):

    k1 = j1 + n_overlap - s1
    k2 = k1 + binsize

    # Filter the signal
    sig_filt[j1:j3] = butterworth_lowpass(signal[k1:k2], freq,
        cutoff, order)[s1:s2]

    # Update indices
    j1 = j3
    j2 = j1 + binsize
    j3 = min(j2 - n_overlap, n_sig)
    s2 = s1 + j3 - j1

return sig_filt

"""
moving_average(signal, binsize)

Function that applies a moving average filter of a selected binsize
to a passed signal. Inputs are the 'signal' to be filtered and the
'binsize' or the number of points averaged in the moving average.
The signal is padded with its initial and final values so that the
moving average does not reduce the signal size. The function
returns the filtered signal, which has the same length as the input

```

```

    signal.

    Written by Thomas Bennett, 2022-01-26
"""
def moving_average(signal, binsize):

    # Get the length of the signal
    n_sig = len(signal)

    # Correct binsize if it is even
    if binsize % 2 == 0:
        binsize += 1

    overlap = int(np.floor(binsize/2))

    # Add buffers before and after the signal
    signal = np.concatenate((np.ones(overlap) * np.mean(signal[0]),
        signal, np.ones(overlap) * np.mean(signal[-1])))

    # Initialize the filtered signal array
    sig_filt = np.zeros(n_sig)

    k1 = 0
    k2 = k1 + binsize

    for i in range(n_sig):

        # Filter the signal
        sig_filt[i] = np.mean(signal[k1:k2])

        # Update indices
        k1 += 1
        k2 += 1

    return sig_filt

```

Appendix D

LabVIEW™ Virtual Instrument for Temperature Measurement

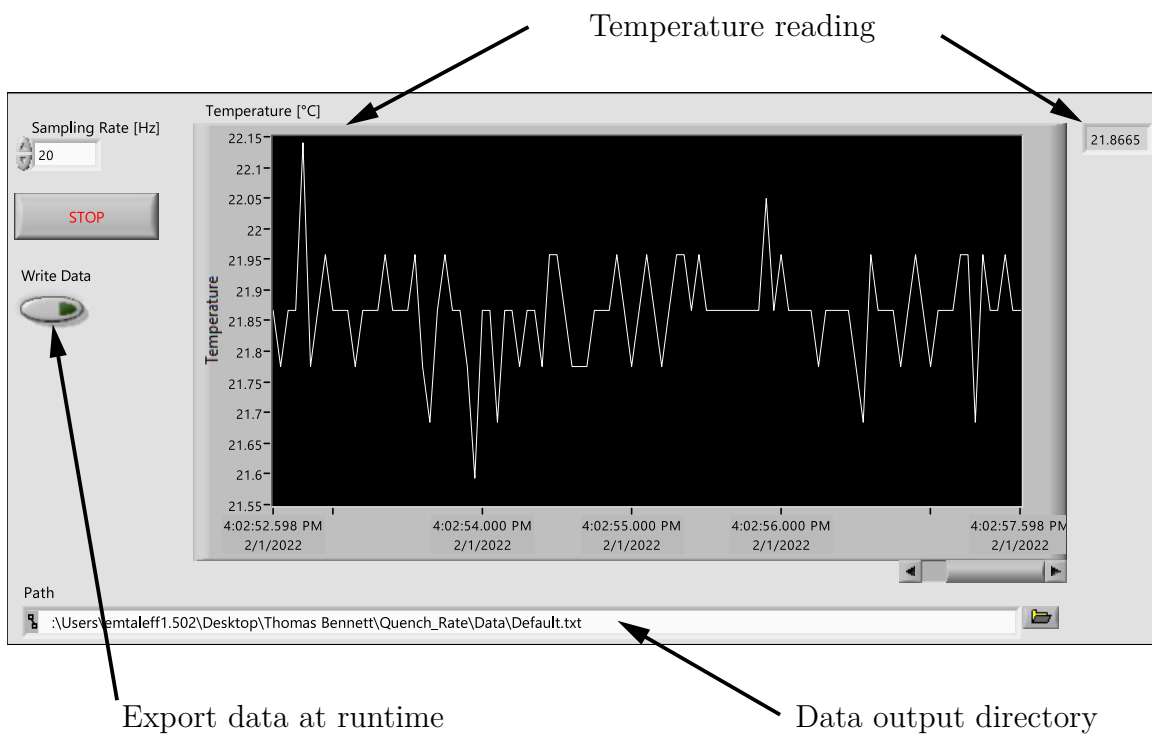


Figure D.1: The front panel of the LabVIEW™ virtual instrument is shown.

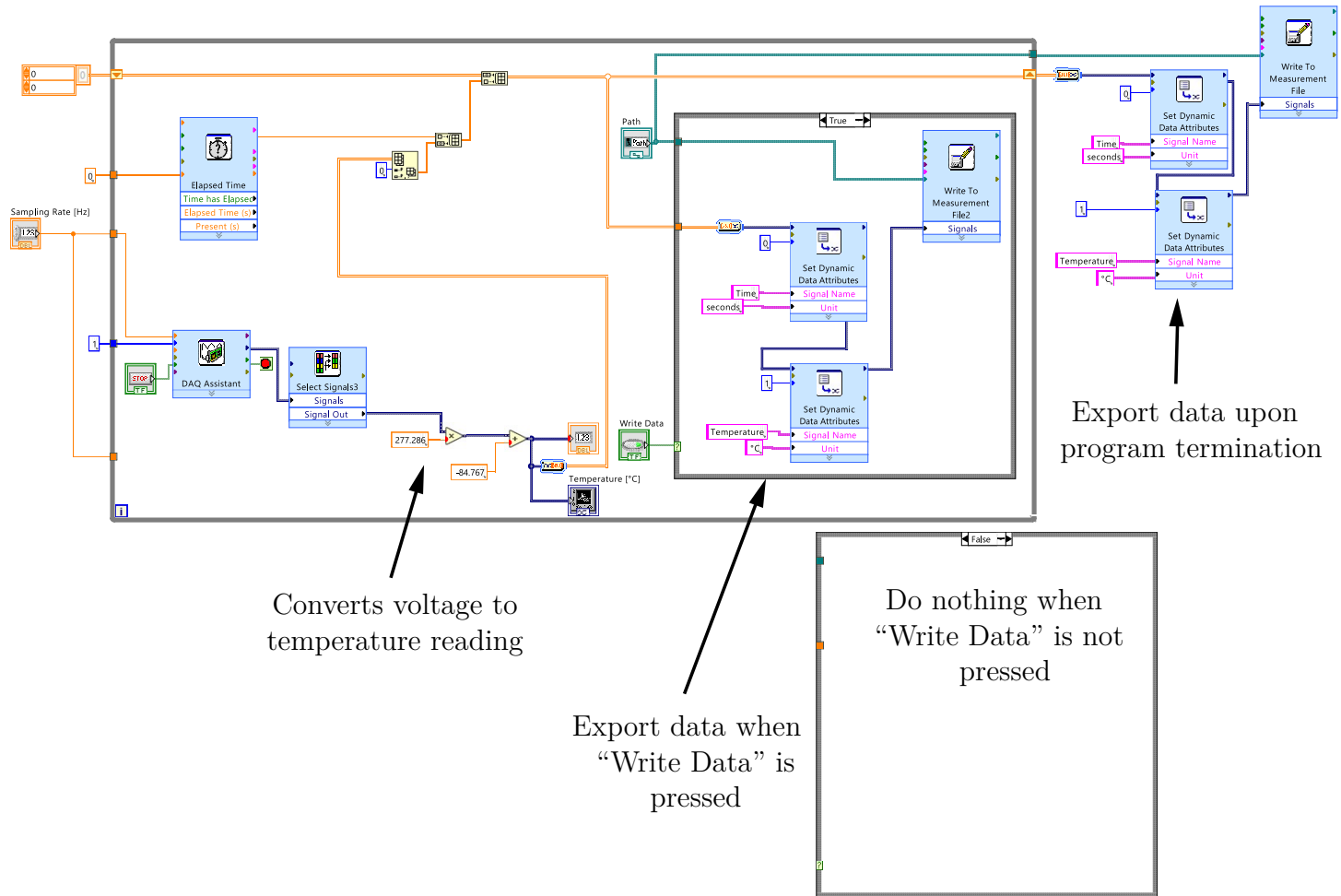


Figure D.2: The block diagram for the LabVIEW™ virtual instrument is shown.

Appendix E

Forming Gas Flow Meter Data

Table E.1 : The flow meter marker locations and corresponding flow rates for N₂ provided as reported by Brooks Instrument for part number 60410_R5.

Marker Location [mm]	N ₂ Flow Rate [cm ³ /min]
2	23.4
3	29.9
4	36.3
5	44.2
6	52.1
7	61.9
8	71.7
9	83.8
10	95.8
11	110
12	124
13	140
14	156
15	173
16	190
17	207
18	225

Continued on next page

19	242
20	259
21	277
22	294
23	312
24	329
25	346
26	363
27	379
28	395
29	411
30	427
31	442
32	457
33	472
34	486
35	501
36	516
37	530
38	544
39	559
40	573
41	587
42	602
43	616
44	631
45	645
46	660

Continued on next page

47	674
48	689
49	703
50	718
51	732
52	747
53	761
54	775
55	789
56	803
57	816
58	830
59	844
60	858
61	871
62	885
63	898
64	912
65	924

Bibliography

- [1] J. Humphreys, G. S. Rohrer, and A. Rollet, *Recrystallization and Related Annealing Phenomena*. Cambridge, MA: Elsevier, 3rd ed., 2017.
- [2] R. E. Rupp, *Dynamic Normal Grain Growth in BCC Interstitial-Free Steel During Hot Deformation*. PhD thesis, The University of Texas at Austin, Aug. 2018.
- [3] N. Yoshinaga, N. Sugiura, and S. Hiwatashi, “A novel texture improving young’s modulus in rolling direction of hot rolled low carbon sheet steel,” *ISIJ Int.*, vol. 57, no. 12, pp. 2263–2265, 2017.
- [4] T. Kataoka, H. Atsumi, M. Yasuda, N. Morishige, and K. Murakami, “Effects of grain boundary characteristics on secondary recrystallization textures in fe–si alloy,” *ISIJ Int.*, vol. 61, no. 3, pp. 960–966, 2021.
- [5] W. D. Callister, Jr. and D. G. Rethwisch, *Materials Science and Engineering: An Introduction*. Hoboken, NJ: John Wiley and Sons, 9th ed., 2014.
- [6] R. E. Rupp, P. J. Noell, and E. M. Taleff, “Creep deformation and dynamic grain growth in an interstitial-free steel,” *Metallurgical and Materials Transactions A*, vol. 51A, pp. 6167–6183, Dec. 2020.

- [7] P. J. Noell, *The Influence of High-Temperature Tensile Deformation on Microstructure Evolution in Select BCC Metals*. PhD thesis, The University of Texas at Austin, Austin, TX, Dec. 2015.
- [8] W. Mankins and S. Lamb, “Nickel and Nickel Alloys,” in *Properties and Selection: Nonferrous Alloys and Special-Purpose Materials*, vol. 2, ASM International, Jan. 1990.
- [9] M. M. Schwartz, “Fundamentals of Brazing,” in *Welding, Brazing, and Soldering*, vol. 6, ASM International, Jan. 1993.
- [10] M. J. Lucas, Jr., “Brazing of Stainless Steels,” in *Welding, Brazing, and Soldering*, vol. 6, ASM International, Jan. 1993.
- [11] M. K. Chaffee, T. J. Hammer, and M. M. A., eds., *Seal Design Guide*. 310 Erie St., Lancaster, NY: Apple Rubber Products, 2000.
- [12] S. Larrabee, “Controlled Atmosphere Chambers,” in *Induction Heating and Heat Treatment*, vol. 4C, ASM International, June 2014.
- [13] Z. M. Shapiro and T. R. Moffette, “Hydrogen flammability data and application to pwr loss-of-coolant accident,” tech. rep., Bettis Plant, Pittsburgh, PA, Sept. 1957.
- [14] J. Rösler, H. Harders, and M. Bäker, *Mechanical Behaviour of Engineering Materials*. Berlin: Springer, 2010.

- [15] H. Oikawa, "Lattice self-diffusion in solid iron: A critical review," *The Technology Reports of the Tohoku University*, vol. 47, no. 1, pp. 67–77, 1982.
- [16] W. Köster, "Die temperaturabhängigkeit des elastizitätsmoduls reiner metalle," *Zeitschrift für Metallkunde*, vol. 39, no. 1, pp. 1–9, 1948.
- [17] ASTM International, "ASTM E 112–13: Standard test methods for determining average grain size," Standard Designation E112–13, ASTM International, 100 Barr Harbor Drive, P.O. Box C700, West Conshohocken, PA 19428-2959, July 2013.

Vita

Thomas Bennett was born in New Orleans, Louisiana. His family relocated to Leander, Texas in 2005 following Hurricane Katrina. Thomas graduated as the salutatorian from Leander High School in 2016. Inspired by his father, Thomas chose to study mechanical engineering at the University of Texas at Dallas. After receiving his bachelor's degree in the spring of 2020, Thomas enrolled in the University of Texas at Austin and joined the Taleff Research Group. After receiving his master's degree in mechanical engineering, Thomas plans to continue his work with the Taleff Research Group and pursue his doctorate.

Email address: tjbennett4th@gmail.com

This thesis was typeset with \LaTeX^\dagger by the author.

[†] \LaTeX is a document preparation system developed by Leslie Lamport as a special version of Donald Knuth's \TeX Program.